

4. Results and discussion

4.1. Macroscopic properties

The use of mesoporous silica films (MSFs) in integrated optics is based on the knowledge of their optical properties. The precondition for it is the detailed knowledge of their macroscopic properties and internal structure. In this Chapter, the MSFs will be first categorized according their visual appearance in order to detect optically perfect films. The objective of the adjacent investigation is to find systematic rules that determine film thickness. For a variety of applications it is very important to control the film thickness. For example, this control could allow one to tune film thicknesses in order to modify diffusion through a porous membrane, to control thermal conductance, or as in this case, to obtain a desirable substrate thickness for optical applications. Finally, an established synthesis field will be presented in order to find out the existence region of the optically perfect films.

4.1.1. Classification of the fabricated mesoporous silica films

According to their visual appearance, two types of the films have been observed after drying and denoted as A-type and B-type. A-type films are perfectly clear, whereas B-type films appear slightly milky. Observation with an optical microscope revealed bubble-like defects between 1 and 100 μm in size for B-type films, whereas the A-type films are fully non-structured (Figure 4.1). An important observation is made if one exposes the A-type films (e.g BTR-BA-089) to a higher humidity (e.g.

2h at RH = 70%) for a certain time before calcination (i.e. before heat treatment of the films). Then, the films transform to B-type films and become milky [112].

After calcination, transparent, crack-free, clear, and mechanically stable A-type films have been obtained up to a thickness of 1100 nm. Thicker films start to peel off from the substrate. The films have been shrunk down to a thickness of $(60 \pm 5)\%$ of the original film thickness (series BTR-BA-017, -020, and -021). Films with stronger shrinkage have also been found (BTR-BA-089) and assigned to partial transformations to B-type films, which exhibit a significantly lower thickness of $(42 \pm 2)\%$ of the original film thickness (BTR-BA-019). In B-type films small star-like cracks occur at the place of the mentioned defects after calcination. Between these cracks the films are clear and thoroughly connected with the substrate. Thicker films show a dense network of cracks and start to peel off from the substrate.

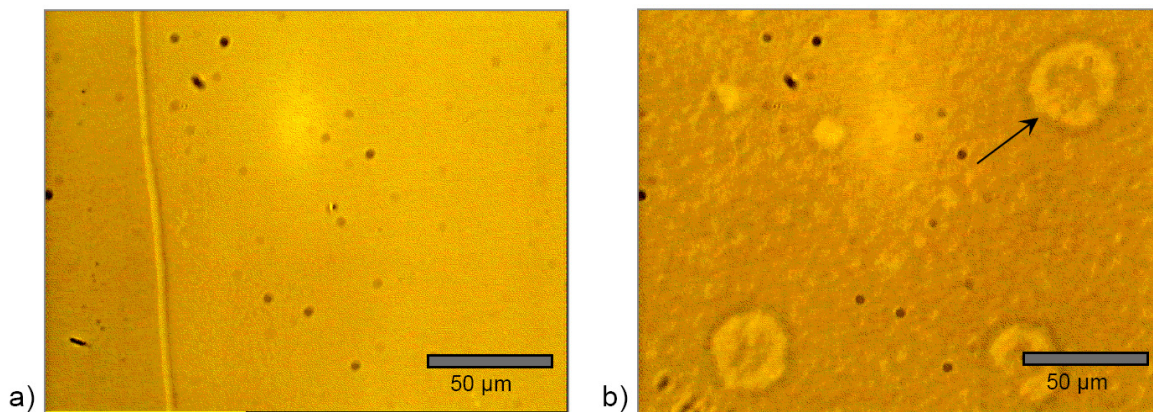


Figure 4.1: Microscope photography of a) an A-type film and b) a B-type film. An arrow indicates a typical defect in the B-type films.

4.1.2. Samples with the homogeneous thickness

In the normal dip-coating process the substrates were withdrawn vertically from the coating solution at a constant speed v . The thickness d of the non-calcined films was varied in the range of 300-2100 nm depending on the used drawing velocity v . The average value of five measured thicknesses is very near to the value measured in the middle of the film, since the film thickness slightly but homogeneously increases in the coating direction. The thickness variations of the samples (KOD-KA-034 and -035) are up to 3%.

In order to examine the influence of the drawing velocity and the ageing of the solution on the film thickness, several films (series BTR-BA-153, -154, and -155) were synthesized from the same coating solution. The solution has been aged for 1, 7 and 14 days at 20°C, and the films were deposited identically.

Figure 4.2 shows the dependence of the film thickness d on the drawing speed v for the calcined A-type films. Lower speeds result in thinner films, while higher speeds give thicker films, as expected. Longer ageing time of the coating solution leads to slightly thicker films. The reason is very likely the increased viscosity of the solution upon solvent evaporation. A law of the type $d = \text{const} \cdot v^{2/3}$ in correspondence to the formula (2.2) has been fitted to the experimental data and found to be in good agreement with the measured data (red line in Figure 4.2). For the more accurate determination of the $d(v)$ dependence more samples synthesized with different drawing velocities at the same processing parameters are needed. This was achieved with the samples coated with a tilting movement as it will be presented in the next section.

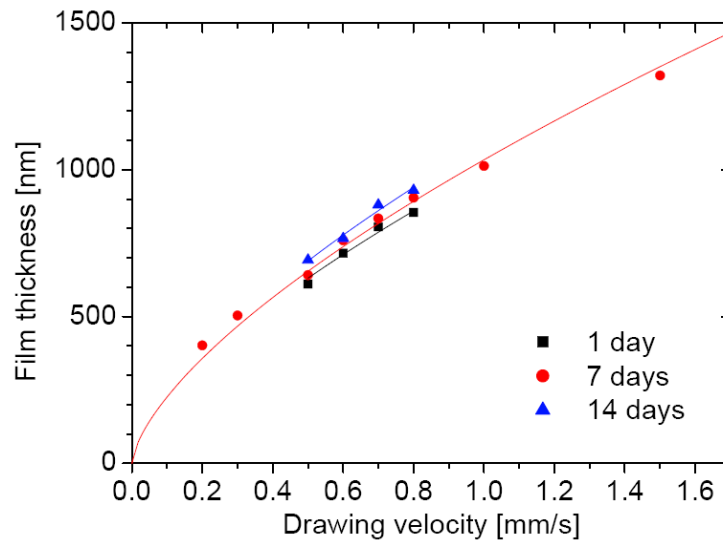


Figure 4.2: The dependence of the film thickness on the drawing rate v . A dependence of $v^{2/3}$ has been fitted to the experimental data obtained for solutions aged after preparation for 1, 7, and 14 days, respectively [113].

The Landau-Levich theory [49] assumes constant Newtonian viscosity and ignores the effects of evaporation during coating. The increase of concentration upon evaporation progressively increases the viscosity. Viscosity changes during

the deposition can explain the finding that the film thickness slightly increases in the coating direction. The slight differences between theory and experiment may additionally be caused by non-ideal free surface behavior. The shear stress is not zero there, because the surface is not ideally extensible [10].

The ageing time of the precursor solution should be controlled since the condensation degree of the inorganic oligomers upon solvent evaporation can influence the mesostructuration. Therefore, the coating solution was used for maximal three coatings after preparation.

4.1.3. Samples with thickness gradients

The samples coated with a tilting movement exhibit a thickness gradient, as it can be seen in the photograph in Figure 4.3. The iridescent colors appear due to interference of the light in the thin film with varying thickness.

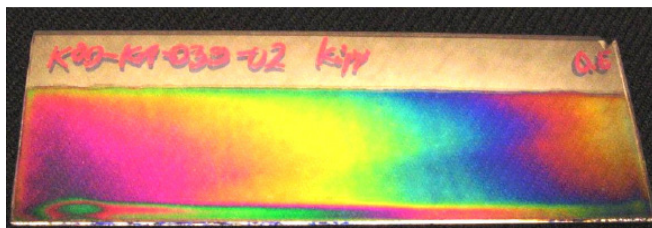


Figure 4.3: Photograph of a sample (KOD-KA-039-02) with the thickness gradient made using a digital camera (Canon PowerShot A520 at 180 dpi, illumination time of 1/100 s, and an aperture F4) at diffuse sample illumination by reflection of halogen light on white paper. The contrast and brightness of the picture were automatically adjusted. The iridescent colors are visible as an effect of the interference of the light in dependence on the film thickness. The appearance of colors deviates from the natural impression.

The thickness distribution in these samples was measured by moving the sample with an x-y stage and driving the interferometer in 3D-mapping mode. An example for the mapping of the sample with a thickness gradient is shown in Figure 4.4. The thickness is biggest at the left side of the sample, at which the substrate was withdrawn from the solution with the highest velocity. The thickness homogeneously decreases to the right side, which is closer to the pivot (see Figure 3.1). The region of inhomogeneities in the thickness mapping on the left side can be correlated with the peel off region from the optical observation. The critical film

thickness, over which the films start to peel off, has been determined to $d_{cr} = 1000 - 1100$ nm for the A-type films.

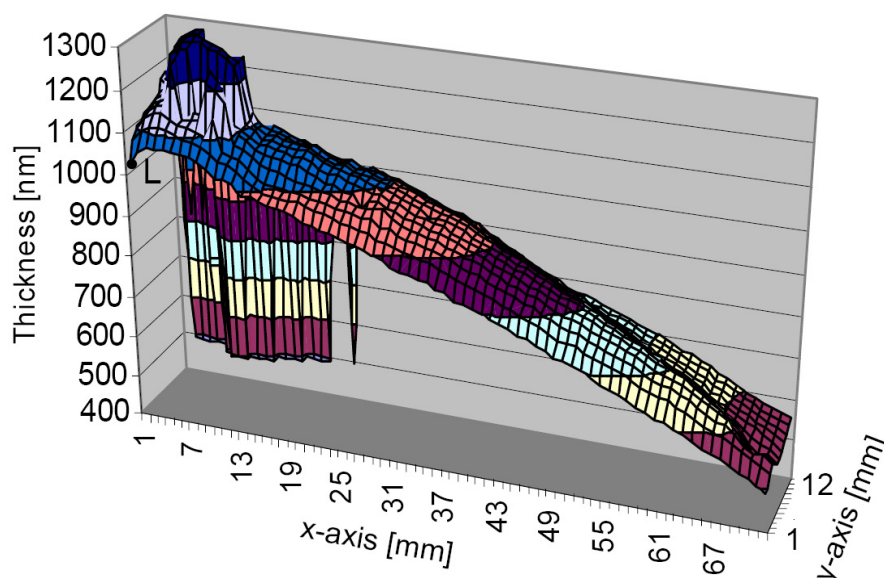


Figure 4.4: An example (KOD-KA-038-03) of the x - y mapping of the film thickness for samples coated with a tilting movement. The point L corresponds to the upper left edge of the sample. At a certain critical thickness the film starts to peel off from the substrate causing an irregular thickness as seen on the left side of the diagram.

The respective drawing velocity was assigned to every measured point with a certain thickness using the equation (3.1). A double logarithmic plot of the film thickness versus assigned velocity is depicted in Figure 4.5. The slope determined from the linear fit is 0.627. The error was estimated from the slope of extremal straight lines to ± 0.03 . The drawing velocity for this particular sample at the point L was $v_L = 1.4$ mm/s. Exponents determined for samples with different drawing velocities v_L are given in Table 4.1.

Table 4.1: Exponents determined for gradient samples with different drawing velocities.

Sample code	Drawing velocity v_L	Rel. humidity	Exponent
KOD-KA-055-06	0.8 mm/s	31 %	0.618 ± 0.040
KOD-KA-039-04	1.0 mm/s	21 %	0.681 ± 0.030
KOD-KA-043-09	1.4 mm/s	41 %	0.613 ± 0.040
KOD-KA-045-06	1.5 mm/s	31 %	0.648 ± 0.030

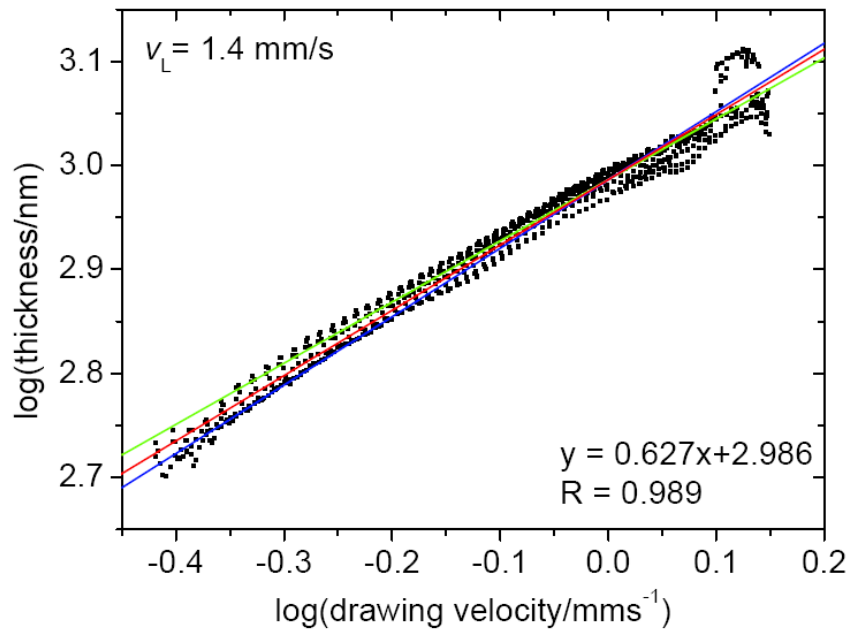


Figure 4.5: Power law fit to the dependence of film thickness on drawing velocity v_i for a film prepared by the tilting movement (KOD-KA-038-03, RH = 32 %, the same sample as in Figure 4.4). The slope of the fit line (red) is 0.63. Blue and green lines are extremals chosen by visual approximation for the estimation of possible errors.

The average value for the exponent α in the expression $d = \text{const} \cdot v^\alpha$ is $\alpha = 0.637 \pm 0.044$. The error is the maximal abbreviation of the determined exponent from the average value. It suggests that the $2/3$ power shown in Equation (2.2) is the appropriate model for this system.

For other mesoporous silica films in a recent work of Tolbert et al. [114], a dependence of $v^{1/2}$ has been found to be closer to the experimental data. However, the drawing velocities in this work are about ten times higher. This is likely the main reason, why their findings better fit to the first regime described in Chapter 2.5.2. They also found out that the variation in liquid vapor surface tension is very small upon the variation of the alcohol to surfactant ratio. It is assumed that the interface contains a monolayer of surfactant molecules regardless of the concentration producing approximately the same surface tension.

In conclusion, this method of coating with a tilting movement is a suitable method to obtain samples with a thickness gradient. In this way the influence of many processing parameters during deposition can be excluded. The exponent for

the dependence of film thickness on the drawing rate has been determined as $\alpha = 0.637 \pm 0.044$. Therefore, the Landau-Levich theory [49] seems to describe this system of mesoporous silica films well.

4.1.4. Synthesis field

The relative humidity turned out to be the most important processing parameter, which determines the film type. In order to obtain perfect A-type films it is crucial to keep the relative humidity on a low level during the synthesis. To achieve the low humidity conditions, an air conditioner and a dehumidifier were used. Additionally, the humidity in the coating chamber was lowered by flushing with dried air, which had been dehumidified in the cooling trap. In this way humidity about 22% below the relative room humidity was reached.

For the measurements of the relative humidity a mechanical hygrometer was used first, and later a calibrated digital one. All the data measured with the mechanical hygrometer were corrected to the calibrated humidity with the standard deviation of $\pm 2\%$ RH. During the film deposition the relative humidity in the chamber fluctuated about $\pm 4\%$ RH, due to opening of the chamber for the sample exchange.

The realized film thickness and the relative humidity during the film deposition form a synthesis field depicted in Figure 4.6. Single points in the diagram represent the samples synthesized with the normal dip-coating with the averaged or central film thickness. The lines in the diagram represent samples deposited by a tilting movement of the substrate. This process results in the broad range of the thicknesses at a certain value of the relative humidity.

One can distinguish three regions in the diagram. Clear A-type films (black circles) appear predominantly in the region of relative humidities below about 41% RH and thicknesses below about 1000 nm (green region). B-type films (blue diamonds) appear predominantly in the region above about 44% RH and with thicknesses below about 970 nm (blue region). Films with ablations for both film types (red stars) are mainly to be found in the region above 1100 nm (red region). In white regions none of these regions could be precisely assigned. The region between A-type and B-type of 4% RH width, where both film types occur, can be

explained with the typical fluctuations of the relative humidity ($\pm 4\%$) during the film synthesis, which is an error of the RH assignment [115].

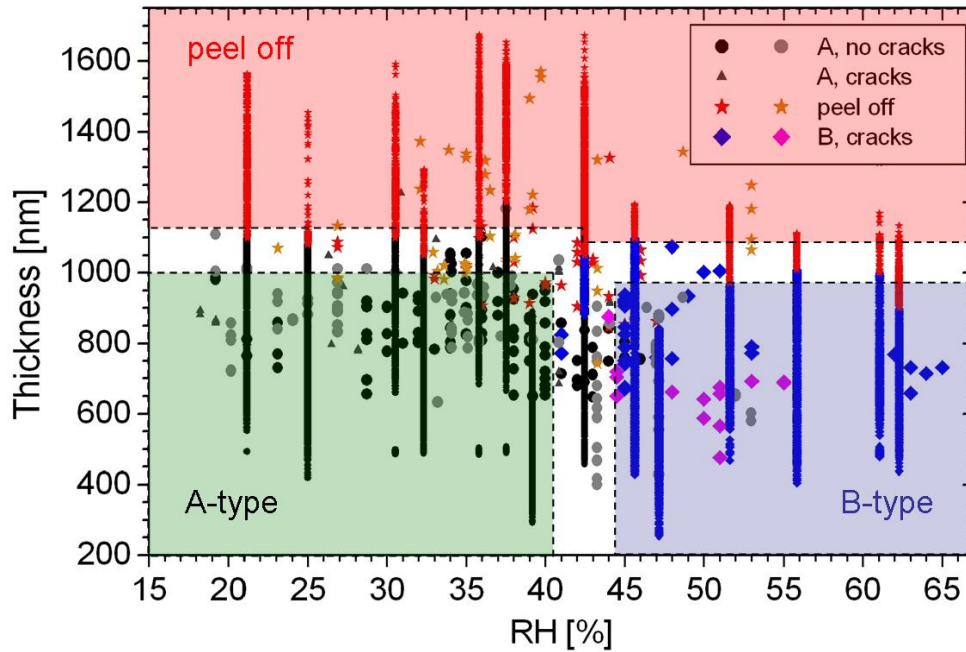


Figure 4.6: Synthesis field: Green region shows thicknesses of the A-type films synthesized at lower relative humidity, blue region: B-type films at higher RH, red region: films with higher thickness, which start to peel off [115]. Black, red, and blue symbols represent the samples from the KOD-KA series; gray, orange, and magenta are the samples from the BTR-BA series (see Appendix).

A few exceptions in the assignment of the film type to the samples synthesized at certain humidity are the transformed B-type films. These samples were fabricated at low humidity but were exposed to air with higher humidity before calcination. It is possible that also some other hidden parameters influence the film type. It was observed that with the fresh solution the A-type films can be synthesized at higher humidities than usual, whereas with the longer ageing time the probability of the occurrence of B-type films becomes higher. A very important step in the film fabrication is the cleaning of the supports. The smallest impurities on the surface can cause thickness deviations and cracks.

An established synthesis field is a very useful tool for the prediction of the film type by knowledge of the relative humidity and the drawing velocity, and thus the final film thickness. It proves the necessity to keep the humidity low during the synthesis in order to obtain optically perfect A-type films.

4.2. Structure determination of the MSFs

In accordance with these findings the question arises, whether these two film types with different macroscopic properties have different internal structures. To determine the nanostructures, small angle X-ray scattering (SAXS), transmission electron microscopy (TEM), and atomic force microscopy (AFM) investigations were performed on both film types and will be presented in this Chapter.

4.2.1. 2D SAXS

Small angle X-ray scattering (SAXS) measurements were performed at different grazing incidence angles ω between 0° and 2.2° . The patterns in Figure 4.7 were recorded at $\omega = 0.3^\circ$ after the accumulation time of 10 hours [112]. They are a selection among the measurements [116] in which the reflections of the primary beam on the interfaces are not pronounced. The right sides of all patterns are screened with the samples, which are positioned nearly perpendicular to the image plane in vertical direction.

Measurements on as-synthesized A-type films deliver a circle-like diffraction pattern with a radius of $2\Theta = 1.08^\circ$ and an isotropic intensity distribution (Figure 4.7 a) besides some pronounced parasitic scattering of the primary beam on the pinhole and the beam-stop. The periodicity or d -spacing is calculated to $d_s = 8.2$ nm using the Bragg equation:

$$d_s = \frac{\lambda}{2 \sin(2\Theta/2)} \quad (4.1)$$

This pattern turns into an ellipse with the same short half-axis of 1.08° (8.2 nm) and a long half-axis of 1.95° (4.5 nm) for calcined films (Figure 4.7 b). The ellipse has a high ellipticity of 1.81. Due to the small diffraction angles involved (commonly below $2\Theta = 2^\circ$), the Bragg equation needs to be corrected for the effect of refraction at the air / film interface. The angle of refraction becomes smaller than the angle of incidence Θ_{obs} , and the Bragg equation is modified to [117]:

$$d_s = \frac{\lambda}{2 \sin \left\{ \cos^{-1} (\cos \theta_{\text{obs}} / \cos \alpha_c) \right\}} \quad (4.2)$$

The total reflection occurs up to the critical angle α_c given by

$$\alpha_c = 1.639 \cdot 10^{-2} \sqrt{\rho} \lambda \quad (4.3)$$

where α_c is in radians, ρ is the density of the film in g/cm^3 , and λ is the wavelength in nm. If the density of the silica framework is 2.2 g/cm^3 [118] and the porosity of the A-type film is 59% (determination will be discussed in Chapter 4.3.3) the average density is calculated to $\rho = 0.90 \text{ g/cm}^3$. Therefore $\alpha_c = 0.138^\circ$ and the lengths of the short and long half-axes should be corrected to 8.5 nm and 4.6 nm, respectively.

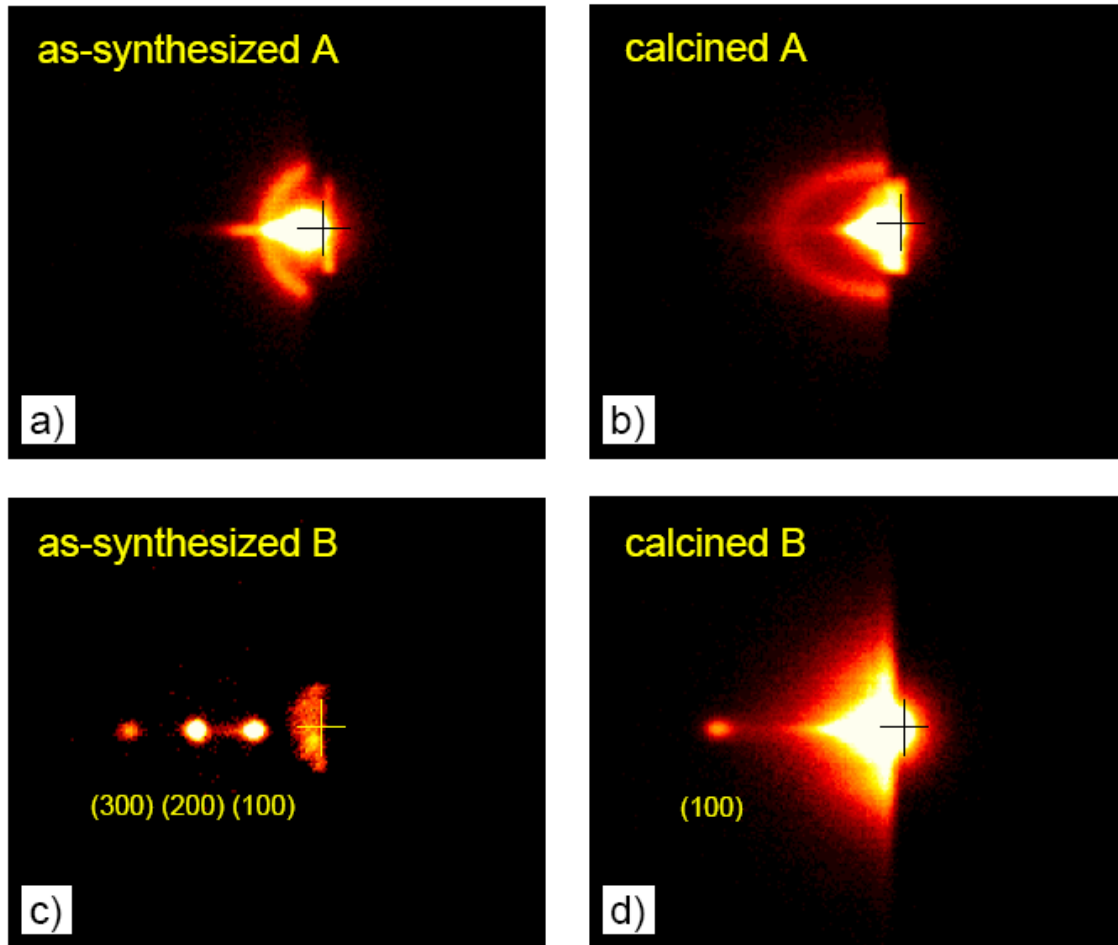


Figure 4.7: The 2D SAXS diffraction patterns of a) as-synthesized A-type (BTR-BA-084-01), b) calcined A-type (BTR-BA-097-01), c) as-synthesized B-type (BTR-BA-067-02), and d) calcined B-type (BTR-BA-089-02) mesostructured silica films. The right sides of these patterns are covered with the sample, which is positioned nearly perpendicular to the image plane in vertical direction. The crosses indicate the position of the non-diffracted beam [112].

The observation of homogeneous diffraction ring for the as-synthesized A-type films reflects an organization of the cylindrical channels into domains, which are not

well-aligned with the film surface [119]. The continuity of the diffraction ring suggests orientation of the channel axes in all directions, but the channels have uniform, well defined pore sizes.

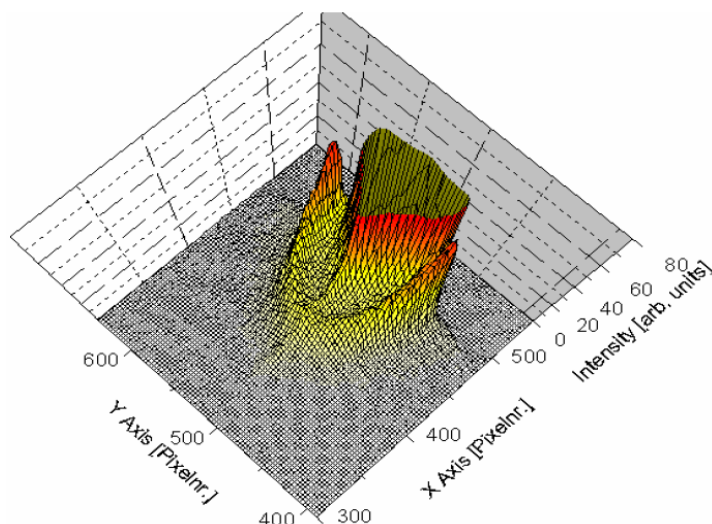


Figure 4.8: 3D view of the intensity distribution in the diffraction pattern of a calcined A-type film (BTR-BA-097-01).

The ellipsoidal continuous diffraction pattern of the calcined A-type films has about three times higher diffraction intensity in lateral direction than perpendicular to the film (Figure 4.8). This diffraction pattern is attributed to a partial ordering of the films with mesostructured domains that have random orientations in the film. After calcination more domains are oriented in lateral direction as it can be seen from the intensity distribution on the elliptical diffraction pattern. This effect can be explained by the unidirectional contraction of the initial mesostructure. There is no shrinkage within the film-plane upon calcination since the film is connected with a solid support in this direction. Therefore, there is no change in the short half-axis. The structure undergoes a large shrinkage in the direction normal to the surface causing the long half-axis in the diffraction pattern. This effect amounts to 55% which is in agreement with the optical measurements of the film shrinkage of $(60 \pm 5)\%$. For the uncertainty of the SAXS data, sample-to-sample fluctuations have to be taken into account, which result in the same estimated error as the optical shrinkage values. Similar anisotropic shrinkage phenomena have also been observed for other mesoporous films [120, 121].

An additional feature in the diffraction patterns is the intense streak in the out-of-plane direction. It occurs due to the specular reflection of the beam on the substrate [120]. The very distinct scattering feature near the crosses, which indicate the position of the non-diffracted beam, is due to parasitic scattering of the primary beam on the pinholes in the collimator and the beam-stop, which is placed in front of the detector in order to protect it from the primary beam.

As-synthesized B-type films show equidistant peaks diffracted in direction perpendicular to the film plane (Figure 4.7 c). All scattering out of this plane can be assigned to noise or parasitic scattering. The three visible spots can be indexed as (100), (200), and (300) reflections. This pattern is recorded at grazing incidence with an angle of $\omega = 1.1^\circ$ in respect to the film plane fulfilling the reflection conditions more or less for the all visible peaks.

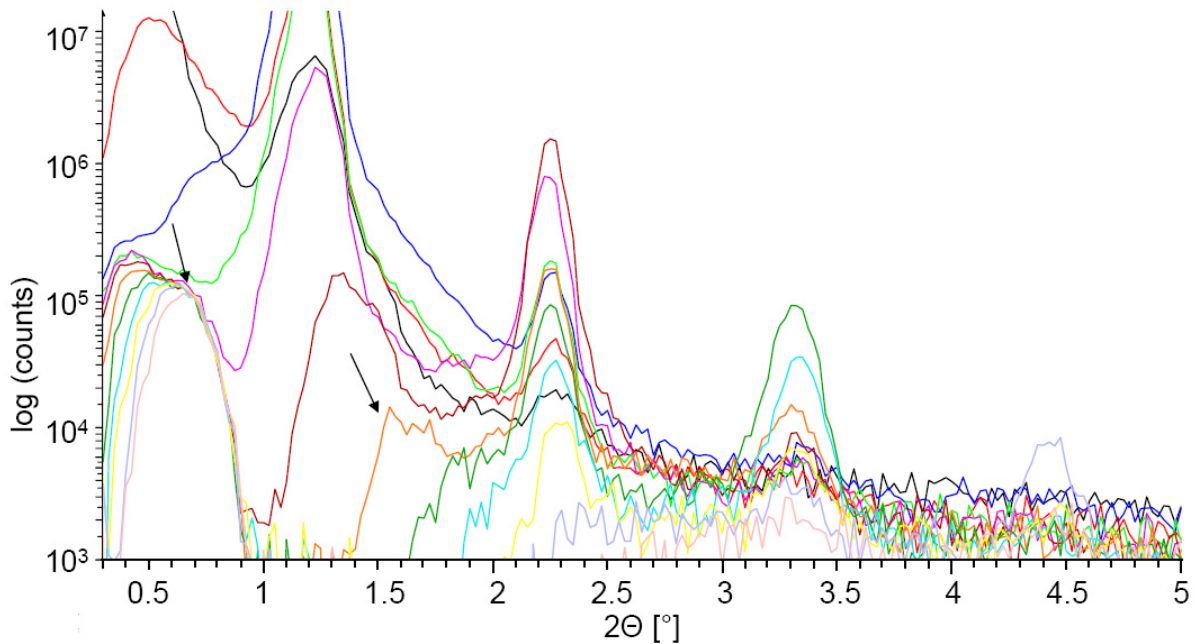


Figure 4.9: X-ray diffraction patterns for an as-synthesized B-type film (BTR-BA-044-06) at incidence angles $\omega = 0^\circ$ (black curve) to 2.2° (pink curve) in 0.2° steps. The arrows indicate two spots, which move by changing the incidence angle ω .

The position of these spots can be determined from the area integration of the set of the 2D patterns recorded at incidence angles $\omega = 0^\circ$ to 2.2° in 0.2° steps (Figure 4.9). Each 2D pattern was recorded for 30 min and integrated in 2θ direction from 0.3° to 5° .

At smaller angles ω two additional spots are visible and move by changing the incidence angle ω in accordance to the law of reflection. They are the result of the reflection of the X-ray beam on the interfaces. The other spots do not change their positions by changing the incidence angle. Therefore, they are true Bragg spots, originated from the X-ray diffraction on the inner structure of the film.

Up to four Bragg peaks are pronounced, at larger incidence angles ω even the (400) reflection becomes visible but the (100) reflection loses its intensity. The positions of the Bragg spots were determined to $2\Theta = 1.2^\circ, 2.2^\circ, 3.3^\circ$ and 4.4° . Therefore, the diffraction pattern indicates a lamellar structure with layers ordered parallel to the film surface. With the porosity of 46% for the B-type films the critical angle is $\alpha_c = 0.158^\circ$ and the layer spacing is calculated using Equation 4.2 to $d_s = 7.9 \pm 0.3$ nm.

The diffraction pattern of calcined B-type films is shown in Figure 4.7 d). Here, one sharp diffraction spot is visible at an angle $2\Theta = 3.1^\circ$. This means that the layer structure parallel to the support remains stable during calcination. The layer spacing is $d_s = 3.0$ nm after Equation 4.2. The large shrinkage in d -spacing to 38% is in agreement with the macroscopic film shrinkage resulting from the thickness measurements.

The diffraction intensity with a “triangular” shape near the beam-stop is another interesting feature to note. It means that the scattering is strongly enhanced in two narrow directions (lateral and normal to the film) and points to enhanced fluctuations in the sample. The absence of higher reflections might be interpreted as a lower ordering, but it can also be connected with the matter distribution in the layer structure.

Rotation of the samples in azimuthal direction φ from 0° to 105° in 7.5° steps and in ω (increase of the incidence angle) from 0° to 1.4° in 0.1° steps did not reveal any additional features.

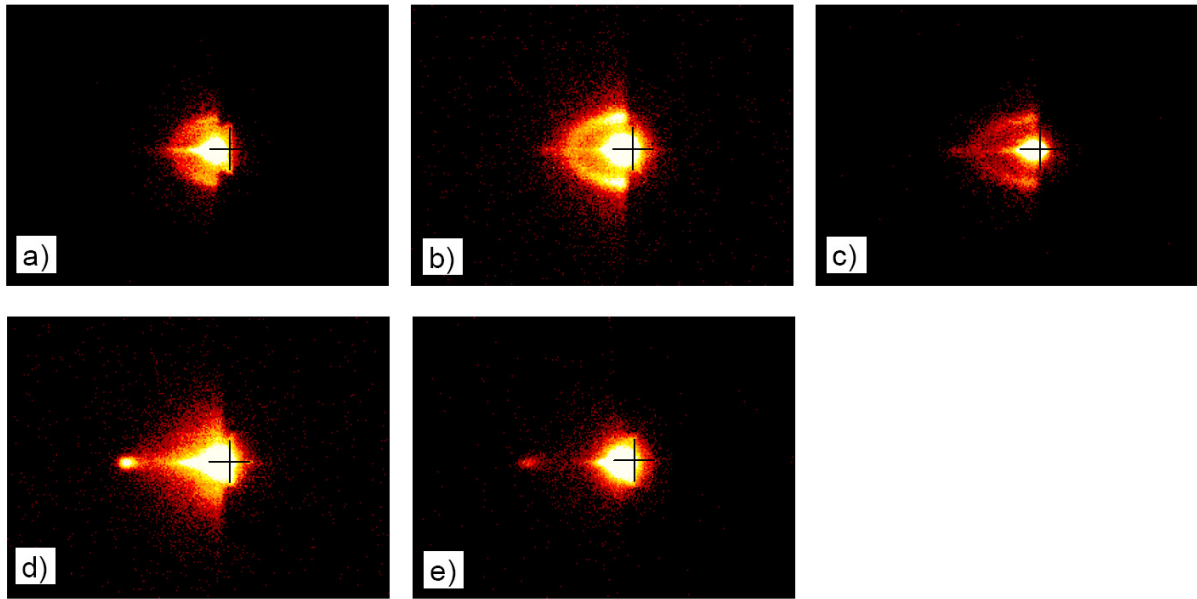


Figure 4.10: The 2D SAXS patterns of calcined A-type films deposited on a) a microscope slide (BTR-BA-017-01), b) a Si-wafer (BTR-BA-037-10) and c) a cover slide (BTR-BA-092-03) and calcined B-type films deposited on d) a microscope slide (BTR-BA-089-02) and e) a Si-wafer (BTR-BA-067-02).

The diffraction patterns have also been investigated for the films deposited onto different substrates, 1 mm thick microscope slides of BK7 glass, Si-wafers, and 0.16 mm thick cover plates (Figure 4.10). Only the two described types of patterns have been found. The intensities of the diffraction patterns differ, very likely due to different accumulation times, but the characteristic features are very similar. The diffraction patterns of all as-synthesized A-type films exhibit circle-like patterns with an isotropic intensity distribution and a radius of $2\Theta = 1.08^\circ$, which corresponds to the d-spacing of $d_s = 8.2$ nm. Also in the case of as-synthesized B-type films, the diffraction patterns exhibit the same distances of the Bragg spots, which correspond to the layer spacing of $d_s = 8.0$ nm. The diffraction patterns of all calcined A-type films are ellipses with the same short half-axes of $2\Theta = 1.08^\circ$ (8.2 nm) as in the case of as-synthesized films. The long half-axes differ slightly for the films deposited onto different substrates, $2\Theta = 1.76^\circ$ (5.0 nm) for microscope slides, $2\Theta = 1.95^\circ$ (4.5 nm) for Si-wafer, and $2\Theta = 1.86^\circ$ (4.7 nm) for cover slides (Figure 4.10, a-c). The reason for the differences in the half-axis, which corresponds to the direction perpendicular to the film surface, might be the different heat conductivity of the supports and, therefore, a different shrinkage of the films. The position of the sharp

Bragg spot in the patterns of the calcined B-type films is the same for films deposited on microscope slides and on Si-wafer, $2\Theta = 3.09^\circ$. It indicates a lamellar structure with the layer spacing of $d_s = 2.9$ nm.

A calcinable lamellar structure for the B-type films seems to be a contradiction in itself, since one expects a collapse of the interlayer spacing after template removal. The existence of this structure proven by SAXS can only be understood if there is a sustaining network among the layers, which keeps the distance between the layers and prevents their collapse. This idea will be discussed in Chapter 4.2.5. The sustaining network could be also a reason for the same film shrinkage to 2.9 nm, independent from the substrate (Figure 4.10, d-e).

4.2.2. TEM analysis

The transmission electron microscope (TEM) analysis was performed on microtomed slices of the samples. The slices were cut perpendicular to the film surface in order to obtain cross sections of the samples. The resulting micrographs of the calcined A-type films in Figure 4.11 a) show strongly fluctuating patterns. Fast Fourier transformations (FFT) of these pictures deliver patterns similar to the diffraction pattern of the SAXS investigations. The retrieved distances of 7.7 nm and 4.8 nm correspond to the spacings calculated from the SAXS experiments within 6 %.

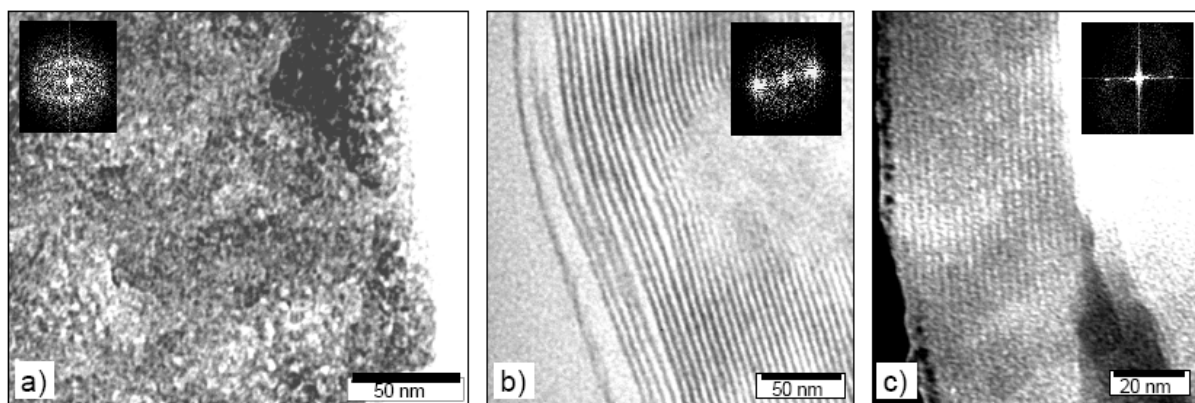


Figure 4.11: TEM micrographs of mesostructured silica films. The cross-sections in normal direction of a) a calcined A-type film (BTR-BA-111-06), b) a calcined B-type film (BTR-BA-109-08), and c) an as-synthesized B-type film (BTR-BA-115-09) are shown. Insets are FFT patterns (modified from [112]).

The micrographs of B-type films show pronounced stripe-like patterns. The distance between the stripes in calcined B-type samples was determined directly from the images and from the FFT patterns. In both cases the distance is $d_s = 2.6$ nm. It is in agreement with SAXS findings within 10%. The stripes are well-ordered and parallel to the film support. A differently ordered pattern has not been observed. Therefore, the TEM results support the lamellar structure found in SAXS. Even a separated layer can be seen on the left edge of the sample in Figure 4.11 b). Tilting the sample in the range of -20° to 20° during the investigation did not reveal any additional structure.

The reasons for the differences (up to 10%) in spacings calculated from the SAXS experiments and TEM micrographs are possibly distortions due to microtoming and embedding effects. An example for the distortions as a consequence of shear forces during microtoming is a separated layer visible in Figure 4.11 b).

4.2.3. AFM

Contrary to the XRD and TEM, AFM is not a standard method for the characterization of the mesoporous materials. It has only been used to obtain the topography and the surface roughness of the thin films. A review is given in [122].

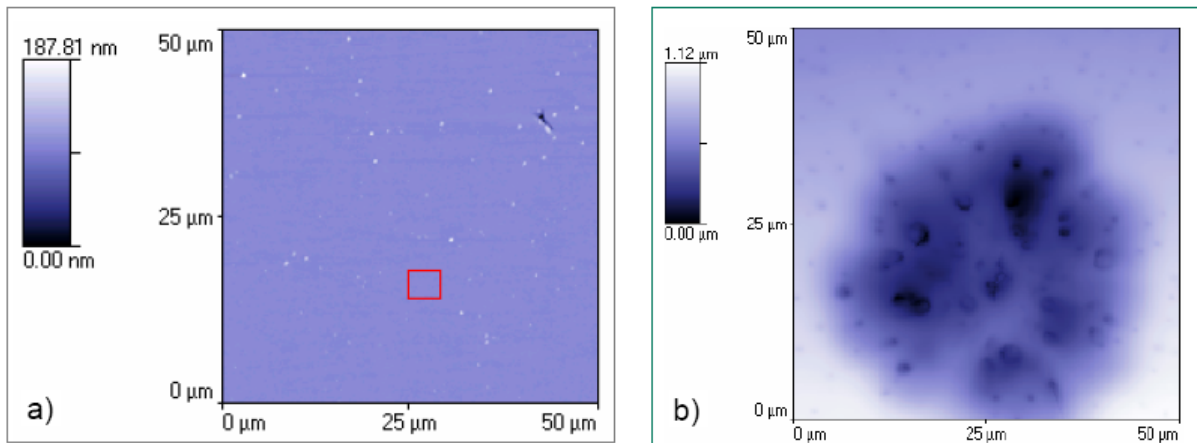


Figure 4.12: AFM height images measured using the ExplorerTM: a) surface of an A-type film (BTR-BA-017-01) (red square marks the region of the RMS roughness measurement), b) typical defect in the B-type film (BTR-BA-044-06).

The softness of the material does not allow the use of the contact mode. The AFM images with lower resolution were obtained using the Explorer™ AFM in tapping mode at the set point of 50%. A silicon tip cantilever with a nominal tip radius of 10 nm was driven at about 251 kHz with the drive amplitude of 0.07 V. Feedback gain parameters were set 1 for integral and 0.25 for proportional gains. The samples were cut and mounted with the double side adhesive tape and scanned with the scan rate of 100 $\mu\text{m/s}$, i.e. 2 Hz. The representative AFM height images of the scan area 50 μm x 50 μm for both film types are given in Figure 4.12.

The topography of the A-type films is fully featureless. All AFM pictures of the A-type films show a very flat surface over the whole film, e.g. with the root mean square (RMS) roughness:

$$\sqrt{\langle \Delta z^2 \rangle} = 0.50 \text{ nm in a } (0.5 \mu\text{m})^2 \text{ region.}$$

The RMS roughness parameter is the standard deviation of the height (z) values in the image.

The bubble-like defects in the B-type films turned out to be depressions with an interesting inner structure. B-type films have also a very smooth surface in the regions without defects, e.g. with a RMS roughness of 0.44 nm. The defects cover approximately 13% of the surface, therein 0.5% are small holes which are not visible with an optical microscope (sample BTR-BA-089-02).

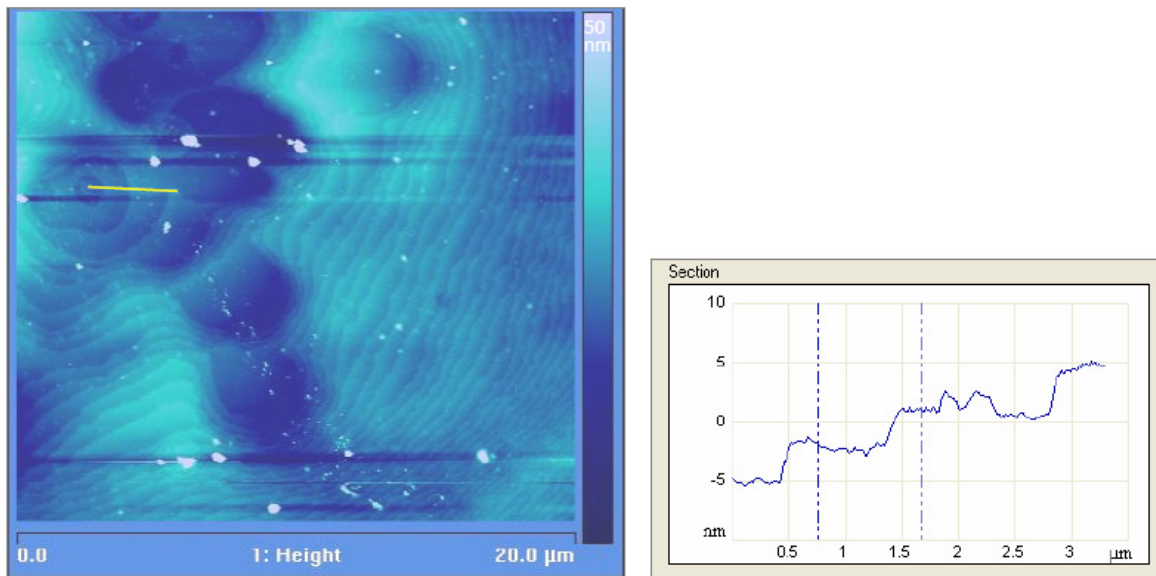


Figure 4.13: AFM image of a defect in a B-type film BTR-BA-067-02 (left). It reveals nano-terraces with a spacing of 3 nm as visible in the section analysis (right).

AFM investigations with higher resolution were performed using two different Dimension 3100 AFMs (Digital Instruments, Inc.). Examination of the defects in the B-type films revealed terraces (Figure 4.13 left). They are visible in about 70% of all investigated defects performing tapping mode. These nano-terraces have a step height of 3 nm, which is in an agreement with the TEM and SAXS results. This value has been measured from the section analysis (Figure 4.13 right) on several places of different samples. The layered structure is clearly visible with lamellae oriented parallel to the substrate. Although the artifacts in the recorded images were reduced by changing the tapping force, varying the feedback parameters, and changing the scan direction and scan speed, there are still some white spots visible. These spots are assigned to some loose debris on the sample surface and dust inclusions. They also caused streaking visible in the image.

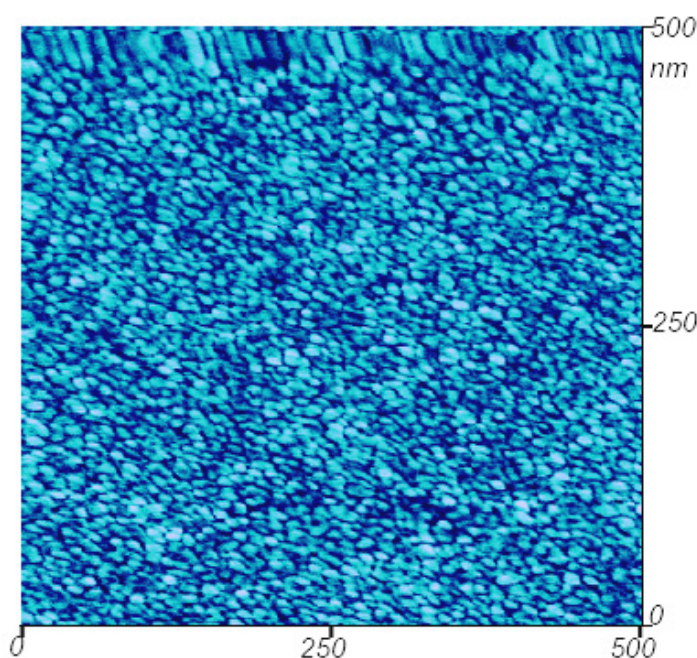


Figure 4.14: AFM phase image of the surface of a calcined B-type film (BTR-BA-067-02). The phase angle variations are in the range 0-20°. The distance between the dark regions is approximately 20 nm [112].

Higher magnification AFM images at 500 nm x 500 nm scan size were recorded in the areas between the defects. Clearly resolved phase images have been found and one example is shown in Figure 4.14. The scan rate of the image was 0.5 Hz and the phase angle variations were in the 20° range with the brightest shade

assigned to 20° phase shift. An irregular dark network, which encloses bright regions of about 20 nm in size, has been found. The stripes on the top of the image are assigned to thermal drift of the sample at the beginning of the measurement.

Similar phase images were also found on several nano-terraces. The height image of a defect topology on the left side in Figure 4.15 gives an overview of the places where the phase images on the right side of the figure were measured.

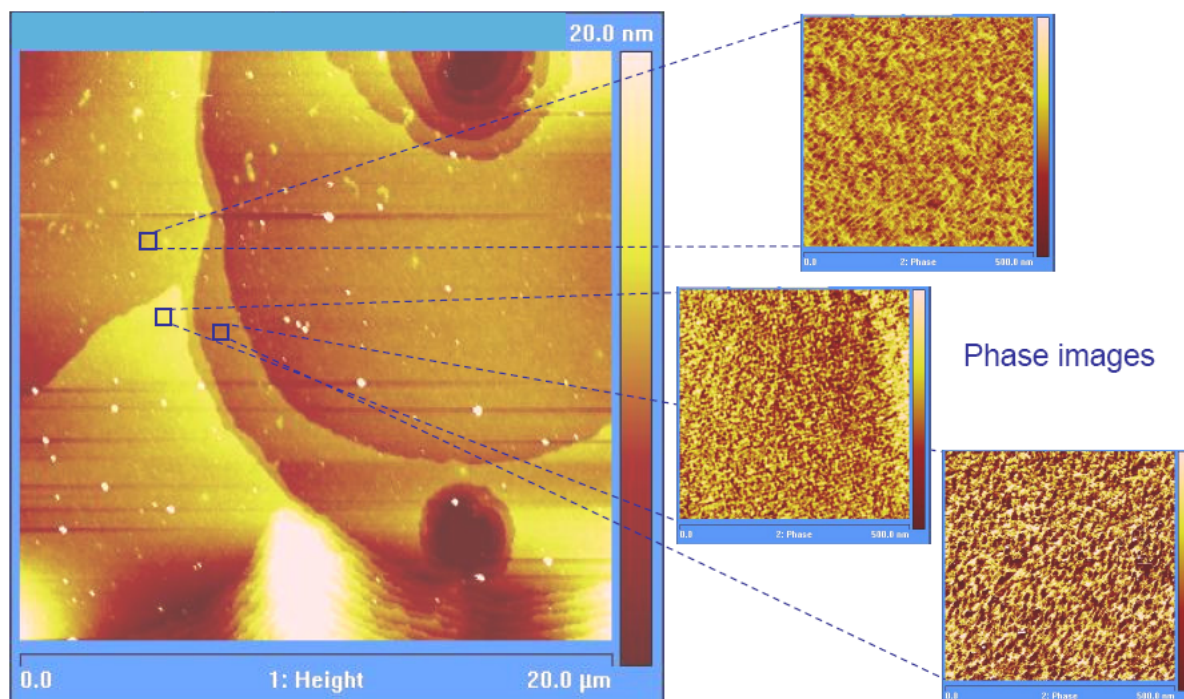


Figure 4.15: AFM height image of a B-type film (left) with marked places on the terraces, where the phase images (right) were measured. The size of the phase images is 500 nm x 500 nm.

Since the z-signal has only low variations, a strong influence of height effects on the phase image can be excluded. Therefore, the phase images were assigned to spatial variation of the energy dissipation, as it has been explained in Chapter 3.3.3. James et al. [103] concluded the color assignment for the tapping mode phase images. With the Digital Instruments phase angle conventions the dark regions with small phase shift have to be assigned to higher energy dissipation. Thus, Figure 4.14 shows a network structure with enhanced energy dissipation. The enclosed bright regions are therefore places, where less energy is dissipated during tip

tapping. This finding gives a substantial hint for the determination of the B-type film structure, which will be discussed in Chapter 4.2.5.

The measured phase shifts for as-synthesized mesoporous silica films are significantly lower (max. 5°) than for calcined films (max. 20°). This fact points to more pronounced dissipation differences in the case of calcined films [112].

4.2.4. The structure of the A-type films

The SAXS patterns indicated a mesostructure consisting of channels with uniform diameters but no alignment in a preferred direction in the as-made form. Upon calcination a shrinkage of the structure in the direction perpendicular to the film surface was observed. Due to the shrinkage, the shape of the channels probably becomes ellipsoidal.

Because only one reflection is visible, no assured assignment to a definite structure is possible. For such an assignment, the TEM results and the consideration of the literature are needed. Dot-like fluctuations of the projected electron density are visible in the TEM micrographs (Figure 4.11 a). They are usually [52] assigned to the wormlike structure [31]. A schematic drawing of the wormlike structure depicted in Figure 4.16 represents a model for the A-type films. This structure can be considered as a non-equilibrium state of a dense-packed channel array. The equilibrium state would be the hexagonal structure.

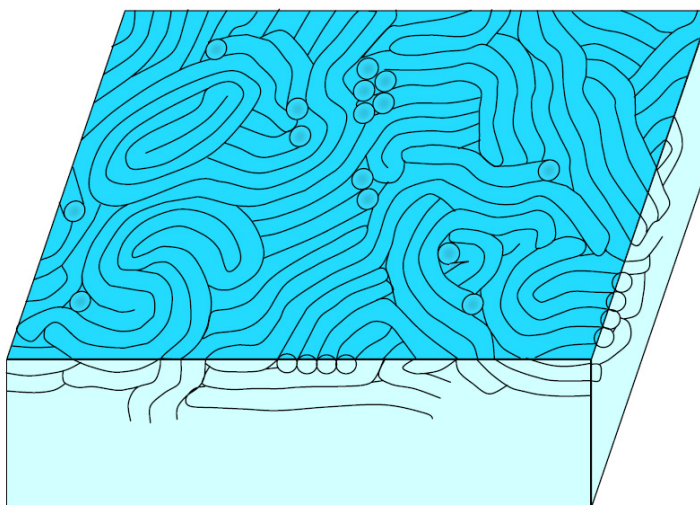


Figure 4.16: Model of the wormlike structure of the A-type films.

It is an interesting question if these films with partially disordered structure can be useful for the application as low- n substrates. Similar films have been reported by some authors [119] but there are no reliable facts that the synthesized films are defect-free and have a sufficient thickness of about 1 μm . For many syntheses [53] it must be recognized that there are unsolved difficulties if the films become thicker than 400 nm. This is, however, too thin for an optical application as a low- n support for the waveguides, because the evanescent fields of the guided wave penetrate deeper into the support.

Much synthesis work was focused on ordered structures [123]. However, these nice and highly ordered structures are not so well suited for surviving the stress during the film synthesis because the structure has no freedom to change without destruction. A partially disordered structure allows a more flexible reaction to the stress during drying, condensation, and template removal. A further advantage of partially disordered films is their isotropy. An advantage of the specific channel-type porosity is the good mechanical integrity.

An advantage of defined mesopores of the investigated films compared to a fully disordered porous system [124] is the possibility of a homogeneous stress distribution in the mesostructure during the fabrication, which allows high film thickness. In addition, the exclusion of large pores results in a very low optical scattering of the films, as it will be shown in Chapter 3.4.4.

4.2.5. The structure of the B-type films

The SAXS patterns and TEM micrographs investigated here clearly show that the structure of B-type films consists of layers ordered parallel to the film surface. They were also made visible in the AFM topography images. But the stability of the structure upon removal the organic structure-directing agent is a very surprising effect. For the detailed understanding of the structure of the B-type films, the AFM phase images should be discussed. The phase image in Figure 4.14 can be interpreted as a map of energy dissipation under the present measurement conditions, as discussed in the literature and summarized in Chapter 3.3.3. But what can such an image mean with respect to the structure of the film?

The calcined film consists of one chemical compound only, which is silica. Thus, the usual explanation in terms of different material hardness [125] seems not to be applicable here. The energy dissipation in AFM tapping mode can result from adsorbed water, bond formation (adhesion) or non-elastic material deformation. The adsorbed water and adhesion part should be position-independent for this material. Therefore, the explanation of the differences in energy dissipation must have its origin in the porous material structure. The non-elastic deformation depends on the internal structure of the material and should be position-dependent.

A porous film with a flat layer on the surface and alternating voids and walls below can be schematically depicted as in Figure 4.17 b). The layer is supported by the walls, which, therefore, can be called sustainers. During tapping of the AFM tip on the film surface the energy is variably dissipated depending on the position. More energy will be dissipated when the tip taps on the fixed sustainer than on the flexible bridge over the void between sustainers.

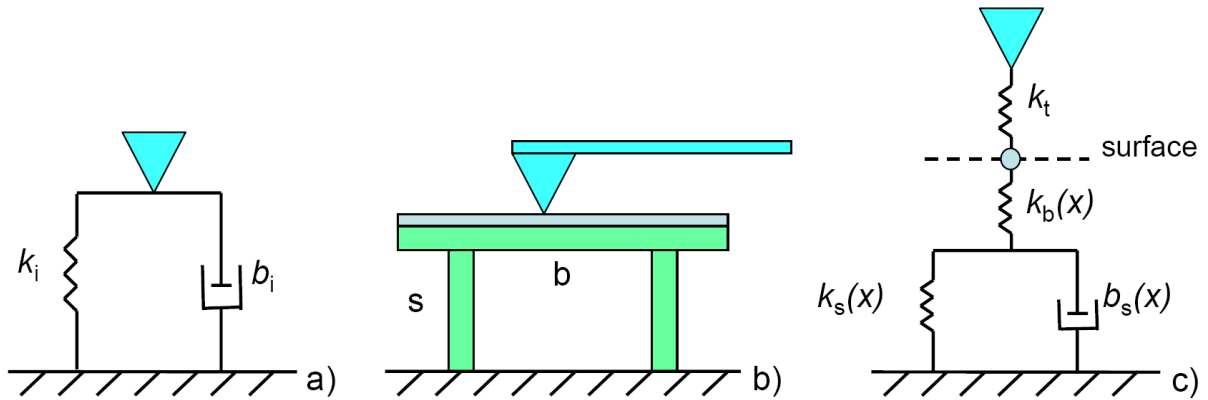


Figure 4.17: a) Scheme of the overall mechanical description of a surface in an AFM experiment. The sample-tip interaction force $F_i = k_i \cdot z + b_i \cdot dz / dt$ consists of a conservative and a dissipative part. b) Surface model of a porous medium. A flat outer surface of a porous medium without external pore openings is described by bridges b and sustainers s . A pore is covered by a bridge whereas a sustainer divides pores and supports bridges. c) Scheme for a mesoscopic mechanical model for a porous medium. The interaction of the tip with the sample is divided into a part describing the force between the tip and the surface (spring constant k_t) and a part responsible for the deformation of the surface (spring constants k_b and k_s , damping constant b_s). k_t is assumed to be independent on the lateral tip position whereas k_b , k_s and b_s are strongly modulated because of the material structure [112].

This assumption (loss-less bending of bridges and loss-producing compressing of sustainers) is used for the construction of a mechanical AFM model for the B-type films, which is shown in Figure 4.17 c). In this model, the dissipation can be calculated and becomes position-dependent (see Appendix 6.3).

The energy dissipation is in this model much larger above the sustainers than between them. This result has two explanations. Firstly, it is more efficient to compress the sustainers directly instead of compressing them via the elastic bridges and, secondly, the compressing of one sustainer is more dissipative than the compressing of several ones simultaneously. Both effects result in the outcome of this model: The regions of higher energy dissipation can be identified with the sustainers between the layers. Therefore, the dark network visible in Figure 4.14 is assigned to the sustaining network, which supports the uppermost layer. The phase images of different layers in Figure 4.15 are similar, but some deviations can occur due to different AFM parameter settings in an automatic adjustment, different relative humidity, and tip quality and contamination.

With the knowledge of the previous discussion, a structure proposal for the B-type films can be made. This sustained lamellar structure is depicted in Figure 4.18. The distance between single layers is kept by the network of sustainers. Flat voids of a typical size of about $20 \times 20 \times 2 \text{ nm}^3$ occur among the layers.

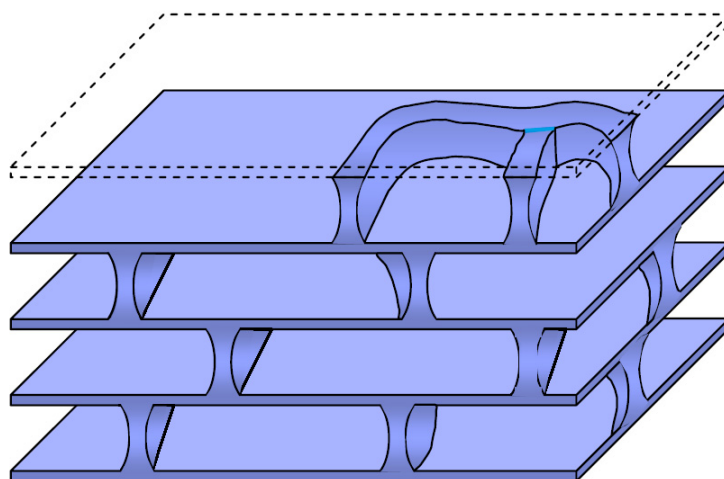


Figure 4.18: Proposed layer structure with sustainers for B-type films [112].

The special structure of the B-type films is very likely responsible for some of their peculiarities. The typical defects can be ascribed to shrinkage problems during film condensation. On a solid support, a parallel lamella has no possibility to relax when it shrinks, except the formation of a defect. Furthermore, single lamellas detached as a consequence of the stress during microtoming have been observed in the TEM micrographs (Figure 2.3). This fact points to a reduced integrity between the lamellas which is consistent with the relatively large typical distance between sustainers of 20 nm.

Other stable lamellar structures, which have been found in vesicle-like inorganic particles [126], should differ from the proposed one (Figure 4.18) by the topology of the sustaining system. Whereas network-like sustaining system is found in B-type films, the sustainers between the vesicle layers should be pillar-like, which can be concluded from the formation mechanism proposed for the vesicles. Very recently, quite similar mesoporous silica films were found by Kuroda et al. [127]. They obtained a weak and broad Bragg peak at $2\theta = 3.2^\circ$ after calcination of the lamellar structure and proposed 2D disordered pores arranged randomly in the layers as rigid spacers among layers. Another group has also recently reported a layered structure where the layers are connected by an ordered array of pillars [117].

The fast Fourier transformations of the AFM phase images did not reveal any ordered structure in the sustaining network. Therefore, the last example can be excluded for our case. Also, the chemical compounds used in [117] are different. But our structure can be considered as a lamellar structure with 2D disordered pores enclosed with sustainers between layers, as it was cited in [127]. The synthesis method described there is very similar to ours. Therefore, a novel structure in Figure 4.18 is a special result of the mesoporous synthesis class.

4.2.6. Stability of the structures

For a potential further processing the films should show high chemical, mechanical and thermal stability. In order to examine the thermal stability, the calcined films were additionally thermally treated. The pieces of the same sample were subsequently heated from 500°C to 1000°C in 50°C steps and examined with small angle X-ray scattering.

SAXS patterns of the films thermally treated at 800°C are shown in Figure 4.19. They are very similar to the patterns of the films calcined at 400°C shown in Figure 4.7. This indicates a high temperature stability of both film types.

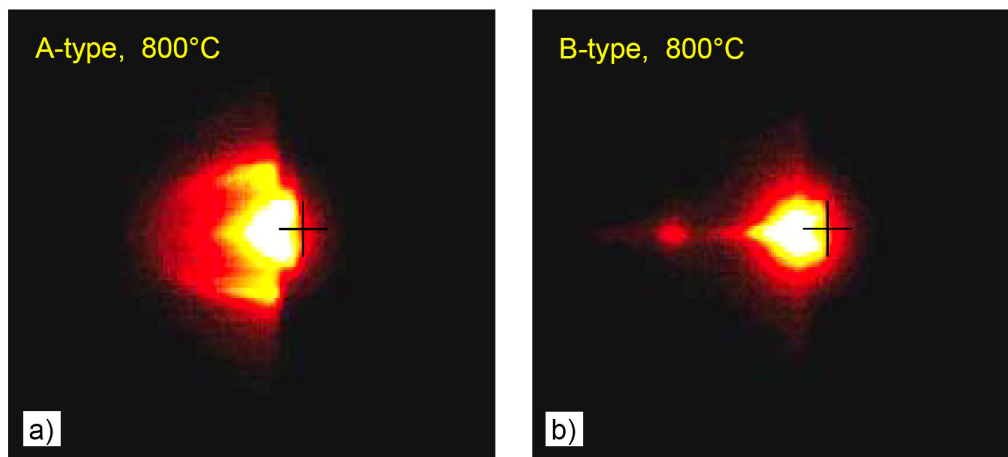


Figure 4.19: The 2D SAXS patterns of calcined a) A-type (BTR-BA-126-05) and b) B-type films (BTR-BA-040-07) heated to 800°C. The patterns were recorded for 1 hour at grazing incidence with an angle of $\omega = 0.3^\circ$ in respect to the film plane [113].

The diffraction pattern of the A-type films is again an ellipse with the half axes of $2\Theta = 1.2^\circ$ and $2\Theta = 2.2^\circ$, which was attributed to the wormlike structure. The corresponding periodicities are after (4.1) $d = 7.6$ nm and $d = 4.0$ nm, respectively. The patterns of all other pieces treated at different temperatures showed no significant differences [128]. The deviation in the short half-axis from the samples calcined at 400°C is 9%, whereas the long half-axis is 11% shorter. The heat treatment leads to the shrinkage of the nanostructure and, therefore, the entire film.

Thickness measurements proved further slight shrinkage during the heat treatment. Between the last two thermal steps, for temperatures between 950°C and 1000°C, the diffraction pattern disappears indicating collapse of the structure. No occurrence of the cracks or film defects has been observed as a result of the temperature treatment [113].

Upon calcination and thermal treatment at 800°C of the B-type films one sharp diffraction spot is still visible at an angle $2\Theta = 2.6^\circ$ (Figure 4.19 b). It corresponds to the layer spacing of 3.4 nm. The deviation from the spacing of the films calcined at 400°C is 11%. The existence of the Bragg spot means that the layer structure

parallel to the support remains stable during the heat treatment. In context of the proposed model (Chapter 4.2.5), this fact means that the sustainers have stabilized the lamellar structure even at the high temperatures keeping the distance between layers. The diffraction spot disappears when the films are thermally treated above 850°C, which shows the final collapse of the structure.

The high temperature stability up to 950°C for the A-type films is more than sufficient for the most of the further processes in which these mesoporous silica films can be used as substrates for the deposition of other materials.

A mesostructure with a good order degree maintained up to 950°C was reported in [129] for the first time. However, the examined films had an orthorhombic mesostructure. Here, at 1050°C the refractive index was 1.46 corresponding to the value of the dense silica. It indicates the pore collapse and complete densification of the films, without any cracking.

4.2.7. On the formation mechanism of mesostructured films

It is very surprising how sensitively the obtained structures depend on processing conditions, especially humidity. In first works with this SBA-15 synthesis class [34, 54, 53] it was still stated, that the surfactants, which act as structure-directing agents (SDA), solely determine the final structure. However, both film types in this thesis have been synthesized from the solution of the same chemical composition, but they have completely different mesostructures. To understand this phenomenon, it is necessary to get a more detailed picture of the formation mechanism.

The main driving force that governs the film formation is evaporation of volatile components, like alcohol, water, or HCl. It is the driving force of the phase segregation, the micelle self-assembly, and the silica condensation. Because of the very short period of time for evaporation of few minutes and very low quantity of materials in these thin films, it is difficult to investigate such systems. The chemical composition of the film changes during the different evaporation steps and the process goes through a series of non-equilibrium states. A schematic picture of the mechanism can, however, be given based on the equilibrium phase diagrams. We have published this view in [113].

The phases formed by the micellar structures, which are relevant for this synthesis class, were described in ternary copolymer-water-oil phase diagrams, e.g. in ref. [130]. Generally “oil” represents a water immiscible component, in this case butanol as a product of the TBOS decomposition. The silica species of the hydrolyzed silicon alkoxide TBOS can be incorporated in this scheme replacing water molecules. The replacement of H_2O molecules is a good first approximation, but in reality there will also be some partially hydrolyzed silicon alkoxide in the system which exhibits hydrophilic and also hydrophobic parts. These amphiphilic species can act as a co-surfactant and increase the micellar curvature. The result is an increased size of the high-curvature phase regions like the hexagonal H_1 phase in the phase diagram. It is schematically indicated in Figure 4.20.

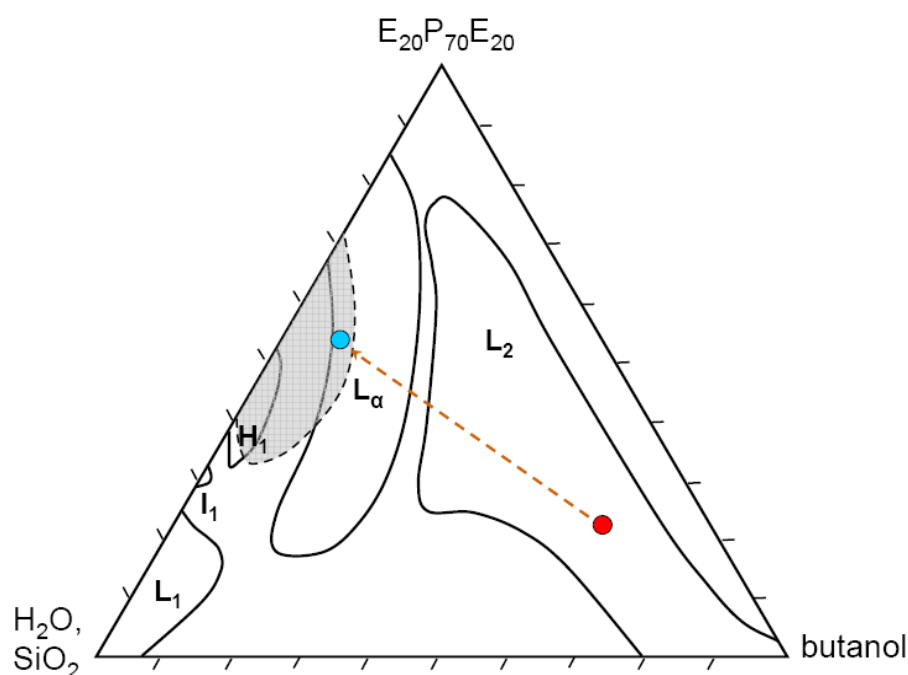


Figure 4.20: Schematic phase diagram of the $\text{EO}_{20}\text{PO}_{70}\text{EO}_{20}$ -butanol-water/silica system with one-phase regions I_1 : micellar cubic, H_1 : normal hexagonal, and L_α : lamellar. L_1 and L_2 denote normal micellar and reverse micellar (water-lean) solutions. Grey region: proposal for H_1 phase changed by co-surfactants. A dotted arrow indicates the pathway from the starting solution to the final film [113].

The chemical composition of the dip-coating solution determines a starting point in this diagram and the end point is given by the composition of the dried film.

Between these two points there is a reaction path determined by the evaporation of the solvents. The starting point can be localized in the region of water-lean reverse micelles in this ternary copolymer-water-butanol phase diagram. Upon butanol evaporation the system tries to approach a point between the lamellar L_α and the hexagonal H_1 phase in the phase diagram. During this time two competitive processes occur: self-assembly and silica condensation. The system will be frozen somewhere on this path in a non-equilibrium state because of the increasing silica condensation. Since a channel-like pore system has been found for the A-type films one can assume that the H_1 phase was approached during solvent evaporation.

The silica condensation is completed upon calcination at 400°C for 10h. If this process is performed directly after film drying, the as-made A-type films are transferred to calcined A-type films. When, however, the films are exposed to higher humidity environment after film drawing, a transformation to B-type films is observed. It is likely that the quantity of water in the films varies with RH and influences the final organization. The still existing partially hydrolyzed silicon species, which act as co-surfactant, will be fully hydrolyzed and repel from the headgroup region of the micelles. The micelles try to lower their curvature and the H_1 region in the phase diagram shrinks. The system tries to approach the L_α state, but since there is already a certain degree of cross-linking in the silica, this transformation cannot be completed. The layered silica phase remains interconnected like the H_1 phase instead of forming a system of separated layers as in L_α . The remaining connections between silica layers form the sustainers discussed in the Chapter 4.2.5. This transformation causes stresses and the layers have no other possibility to relax but to form macroscopical defects visible in Figure 4.1 b). The B-type structure can be considered as an intermediate state of an $H_1 \rightarrow L_\alpha$ phase transformation with remaining sustainers [112].

The synthesis mechanism is very complex because of the non-equilibrium phenomena. It enables different products in agreement with our observations. The careful control of the processing condition appears to be also a theoretical precondition to allow the fine-tuning of the structure.

4.3. Refractive index determination

The refractive index n is the key parameter characterizing the optical properties of a dielectric medium, since it determines the phase velocity of light inside a material. Within this Chapter, a non-conventional determination of the refractive index will be presented in detail.

4.3.1. n -value for A-type films

The refractive index of calcined A-type films was determined from the angle-dependent white light interferometric measurements (see Chapter 3.2.2). The lower side of the sample was measured, whereas the upper side was made “invisible” by a drop of glycerin and covered with a cover slide. One example of the measured transmission spectra for five different incidence angles of perpendicular polarized light (s-pol.) in dependence on wavenumber ν , i.e. reciprocal wavelength, is shown in Figure 4.21. The interference at the thin layer results in different reflection intensities for different wavelengths of light (Fabry-Pérot oscillations). The interference curves have a cosine-like shape with intensity variations of 2-10%.

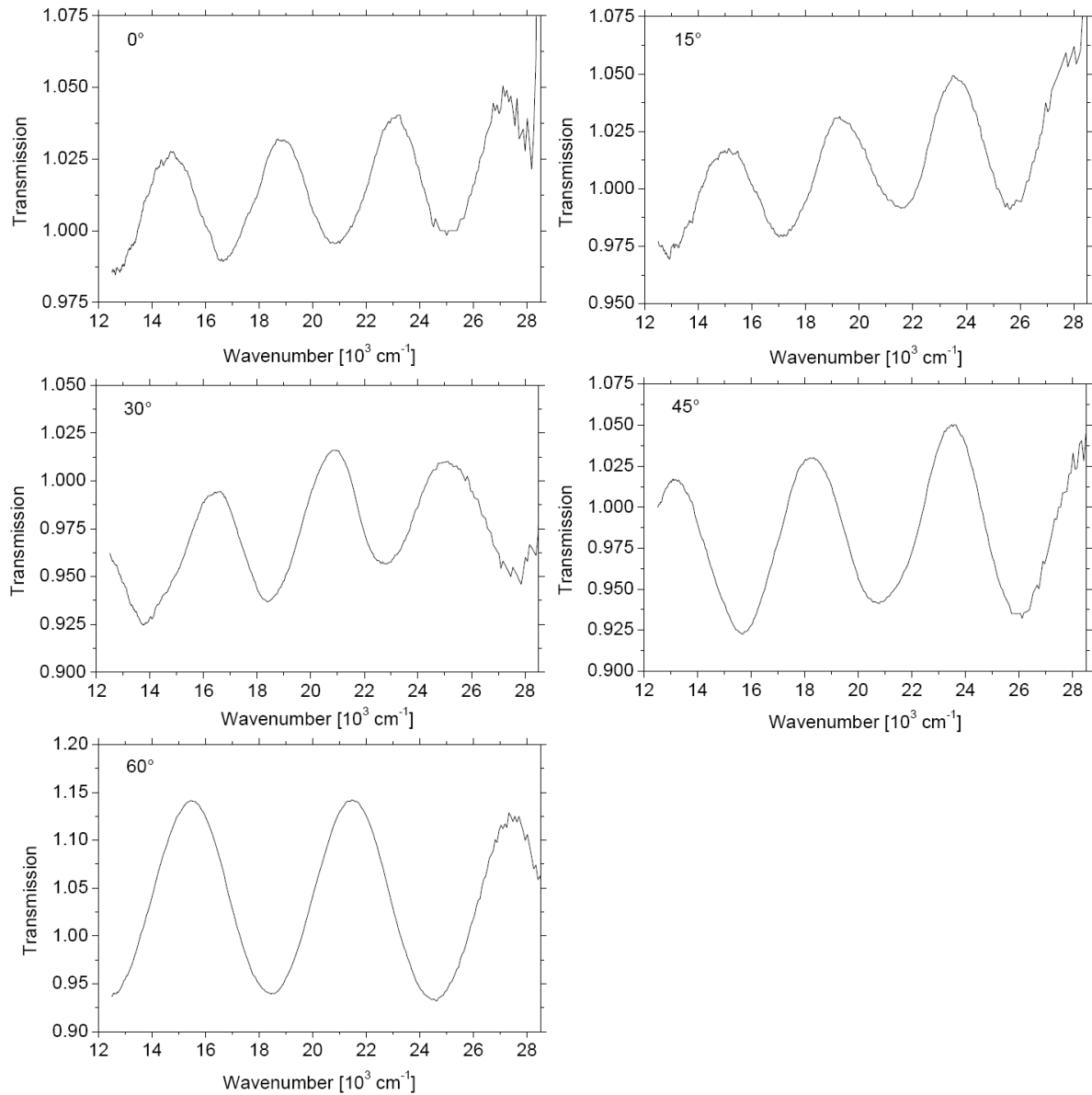


Figure 4.21: Transmission spectra for the *s*-polarized light at incidence angles $\alpha = 0^\circ$, 15° , 30° , 45° and 60° (BTR-BA-029-07).

The positions of the interference extrema on the wavenumber scale have a linear dependence on the interference order due to the periodicity of the cosine function. Therefore, this dependence was fitted with a straight line for each incidence angle (Figure 4.22). Also the maximal and minimal possible values were considered for the error determination. The slope of this line m delivers the thickness dependent part of the optical path difference $\Delta_d = (2m)^{-1}$. It differs from the total path difference Δ by the phase jump due to the reflection on the optically denser medium: $\Delta = \Delta_d + \lambda/2$ [113].

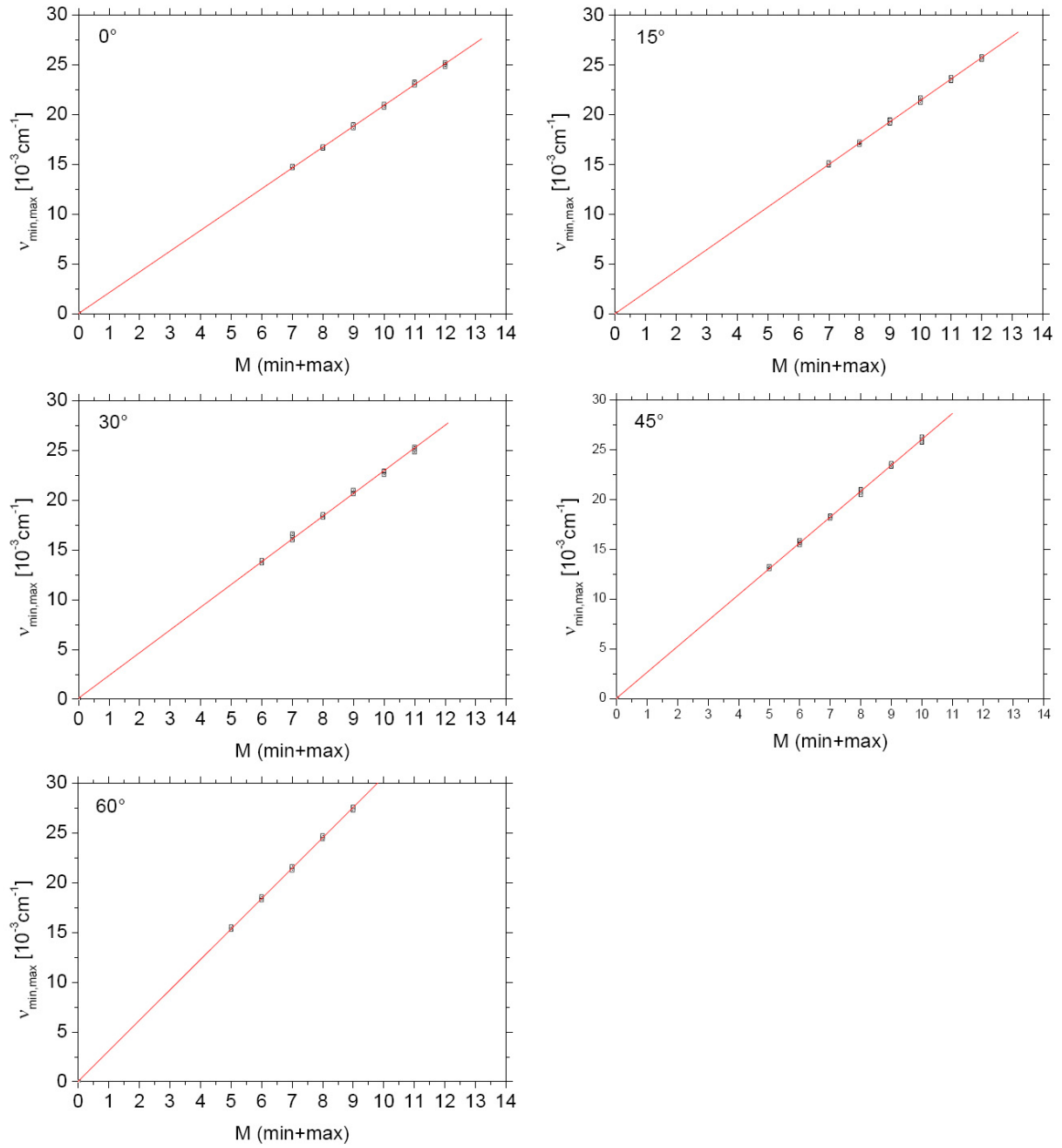


Figure 4.22: Position of the extremum $V_{\min, \max}$ versus the number of the extremum for different incidence angles of s-polarized light for BTR-BA-029-07. The thickness dependent part Δ_d of the optical path difference can be determined from the slope of these graphs.

Figure 4.23 a) shows the dependence of Δ_d on the incidence angle for s-polarized light. It is described by [131]:

$$\Delta_{d,s} = 2d\sqrt{n^2 - \sin^2 \alpha} \quad (4.4)$$

Therefore, the axes have been chosen appropriately to allow a linear fit. This fit enables simultaneous determination of the film thickness d and the refractive index n . A refractive index of $n = 1.187 \pm 0.010$ was determined in the visible range of 350-800 nm. In the near IR region, at $\lambda = 1.3 \mu\text{m}$, a value of $n = 1.14$ was determined by M. Schmidt with a total reflection method on a similar sample [13]. The deviation of 0.04 between the two measurements can be assigned to dispersion or to different small amounts of adsorbed water in the films. For this particular film BTR-BA-029-07, the thickness $d = 1009 \pm 6 \text{ nm}$ is exactly the same as it was determined by the normal white light interferometry. For other films the deviations are within the experimental error of the normal interferometry.

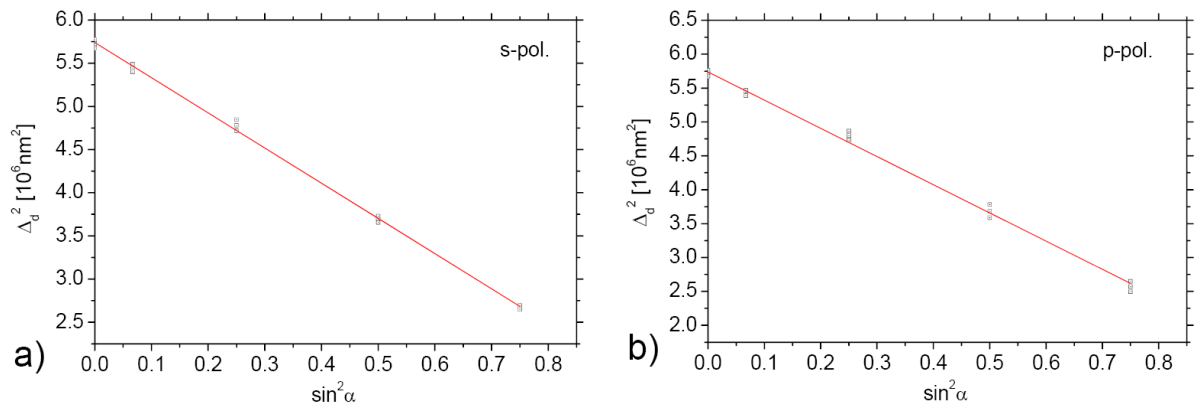


Figure 4.23: Determination of the refractive index n and film thickness for BTR-BA-029-07 from the dependence Δ_d on α for a) s-polarized and b) p-polarized light.

The measurements for the parallel polarized light were performed analogously. In the case of birefringent materials two beams can be distinguished, an ordinary beam with the refractive index $n_s(\alpha) = n_o$, and an extraordinary beam with the angle-dependent refractive index:

$$\frac{1}{n_p^2(\alpha)} = \frac{\cos^2 \alpha}{n_o^2} + \frac{\sin^2 \alpha}{n_e^2} \quad (4.5)$$

It varies between n_o ($\alpha = 0^\circ$) and n_e ($\alpha = 90^\circ$). Angle-dependent optical path difference is therefore:

$$\Delta_{d,p} = 2d \sqrt{\frac{n_o^2 n_e^2}{n_e^2 (1 - \sin^2 \alpha) + n_o^2 \sin^2 \alpha} - \sin^2 \alpha} \quad (4.6)$$

Keeping the values for $d = 1009$ nm and $n_o = 1.187$ the same as for the s-polarized light, the fit for the p-polarized light (Figure 4.23 b) delivers the extraordinary refractive index $n_e = 1.178 \pm 0.005$. The birefringence is thus: $\Delta n = n_e - n_o = -0.009$.

Unfortunately the difference is within the experimental error (± 0.01) and conclusions concerning birefringence of A-type films are, therefore, not possible. However, the X-ray investigations of these films show an anisotropic shrinkage which should lead to a measurable birefringence. For other mesoporous films a low negative birefringence between $\Delta n = -0.005$ and -0.01 [132] was measured as well using spectroscopic ellipsometry.

The refractive indices of other measured samples were e.g. $n = 1.183 \pm 0.003$ for KOD-KA-034-07, $n = 1.166 \pm 0.005$ for BTR-BA-132-01, $n = 1.242 \pm 0.010$ for BTR-BA-154-10, and $n = 1.245 \pm 0.005$ for BTR-BA-142-02. The first two values are in a good agreement with the previous measurement, whereas another two samples exhibit higher refractive indices. Possibly, these samples transformed to the B-type films, because they were exposed to the air with higher humidity before calcination.

Angle-dependent interferometric measurements enable reliable information on the accuracy of the n determination and deliver an n -value averaged over the whole film thickness. It has not been applied to mesoporous films so far.

4.3.2. Influence of ageing and humidity on refractive index

For the application of calcined A-type films as low- n substrates it is important to examine the stability of the refractive index upon humidity changes and ageing. For this investigation the sample KOD-KA-034-07 was first stored in the desiccator at low humidity of about 30% for 107 days and the refractive index was measured with the previously described method to be $n = 1.183 \pm 0.003$. Then, the sample was stored in the desiccator with wet silica gel at 57% RH for 17 days, further 6 days at 97% RH and additional 18 days at 97% RH.

The resulting refractive indices of $n = 1.181 \pm 0.006$, $n = 1.190 \pm 0.017$ and $n = 1.185 \pm 0.012$ respectively, are shown in Figure 4.24.

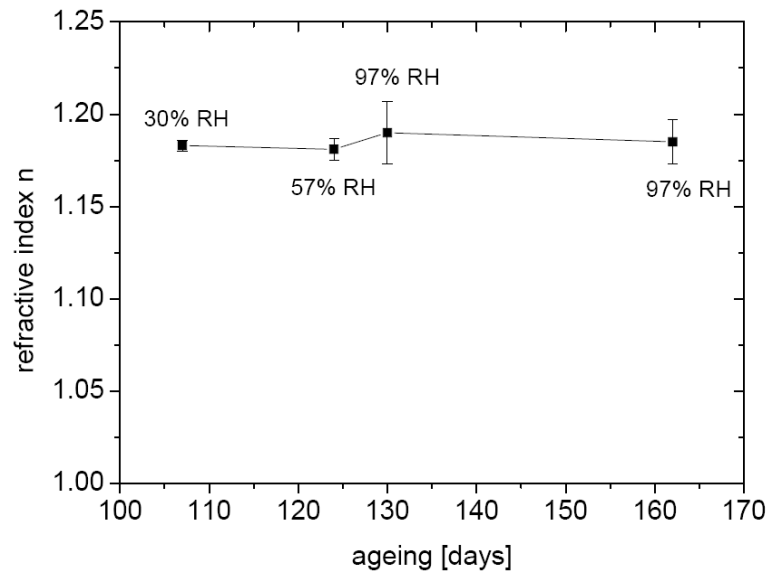


Figure 4.24: Dependence of the refractive index on relative humidity and ageing for the sample KOD-KA-034-07.

It seems that exposition of calcined mesoporous films to higher humidity, as well as the ageing in the period of few months do not influence the refractive index significantly. The measured deviations are within the error bars. However, the error range increases for the measurements after ageing of the sample. Also the determined film thickness increases slightly. This finding could be explained with slight fluctuations of the sample thickness, and with the possibility that the measured area was not exactly the same for each measurement. It is also possible that the optical thickness $n \cdot d$ slightly increases, which is more reflected in the change of d than n due to their strong correlation. This stability at higher humidity is a very important property for a potential use in integrated optics.

Small changes do not necessary have negative effects. Humidity treatments can be even applied to increase the elastic modulus E of mesoporous silica films up to 0.5 GPa without changing the refractive index significantly, as it has been examined in ref. [133]. In any case a collapse of the mesostructure should not occur, but it was not observed with our samples.

4.3.3. Porosity calculation

The volume fraction of air in the films can be estimated by different effective medium theories (EMT) developed from a solution of the Clausius-Mossotti problem [134]. The Lorentz-Lorenz relationship [135]

$$(n_f^2 - 1)/(n_f^2 + 2) = (1 - V_p)(n_s^2 - 1)/(n_s^2 + 2) \quad (4.7)$$

where n_f is the refractive index of the film, V_p is the void volume fraction, and $n_s = 1.46$ is the refractive index of the solid silica framework, delivers a porosity $V_p \cdot 100\%$ of $(58 \pm 2)\%$ for the calcined A-type films.

In this case the volume fractions of the two dielectrics are comparable. Therefore, the effective medium approximation from Bruggemann [136] can be applied:

$$V_p \frac{n_{\text{air}}^2 - n_f^2}{n_{\text{air}}^2 + 2n_f^2} + (1 - V_p) \frac{n_s^2 - n_f^2}{n_s^2 + 2n_f^2} = 0 \quad (4.8)$$

The porosity is calculated to $V_p \cdot 100\% = (59 \pm 2)\%$.

Using a simplified linear effective medium approximation [137] $n_f = n_{\text{air}} \cdot V_p + n_s \cdot (1 - V_p)$ the air filling fraction of the mesoporous films, i.e. the porosity is $(61 \pm 2)\%$. All estimations seem to be useful for the mesoporous silica films since the deviation is within the experimental error coming from the refractive index determination.

The refractive index of B-type films is more difficult to determine because of the pronounced scattering of these films. From the shrinkage of these films during calcination it can be concluded, that the porosity is about 46% and the refractive index must be approximately $n = 1.233$ using Equation (4.7). This value is very near to the refractive indices of the samples BTR-BA-154-10 and BTR-BA-142-02 originally assigned as A-type. It is a good indication, that these samples are transformed B-type films.

In ref. [138] it was discussed in detail, that the effective medium approach is valid for films thicker than up to 50 times the pore diameter. This is always the case for the films investigated here.

4.4. Other properties of the MSFs

Another important applicational aspect of the mesoporous silica films in integrated optics is their very low optical scattering. From their visual appearance, the A-type films do not seem to scatter significantly, but more quantitative conclusions will be derived from the diffuse reflectance measurements in the following section. Possible ionic conductivity of the MSFs will be checked and, finally, important mechanical properties, like elastic modulus and hardness will be presented in this Chapter.

4.4.1. Optical scattering

Diffuse reflectance spectra, measured using a UV-Vis spectrometer with a Praying Mantis™ attachment, show that the diffuse reflectance DR of the calcined A-type films is very low, $DR = 0.13\%$ (red curve in Figure 4.25). This is an average value over the whole measured spectral range of 370-800 nm. However, this value was close to the detection limit of the set-up and may be an overestimation. Since only the scattering in one half-space was collected with the praying mantis, one should consider the scattering S in the whole space: $S = 2 \cdot DR / 100\% = 0.0026$.

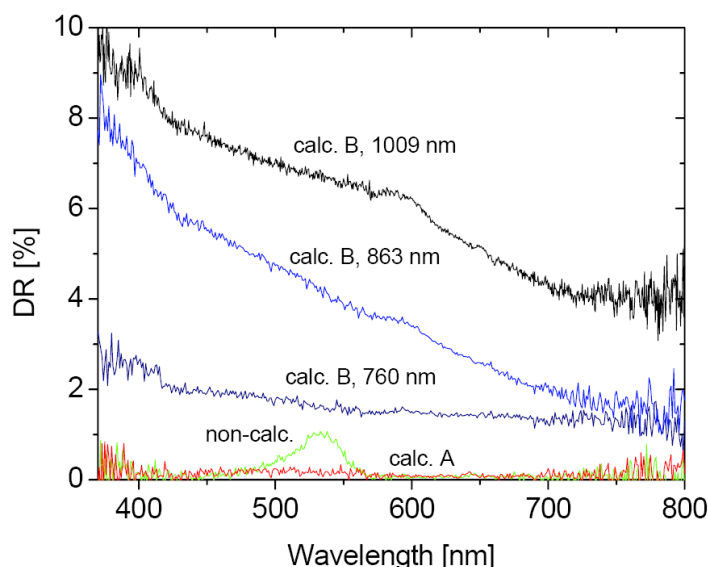


Figure 4.25: Diffuse reflectance spectra of non-calcined and calcined A- and B-type films on microscope slides. Black curve is the sample BTR-BA-089-08, blue BTR-BA-089-09, navy blue BTR-BB-160-08, green BTR-BA-114-03, and red curve is BTR-BA-141-03.

The scattering coefficient α_{sc} was estimated from the measurements of the diffuse reflectance. In analogy to the absorption coefficient $\alpha_{abs} = (1/L) \cdot \log_{10}(P_{\lambda}^0/P_{\lambda})$ [139] with an optical length L and a spectral radiant flux P_{λ} , using the expression $P_{\lambda}/P_{\lambda}^0 = T = 1 - S$, one can determine the scattering coefficient $\alpha_{sc} = -(1/L) \cdot \log_{10}(1-S)$. In this case the film thickness of the A-type film is $d = 863$ nm, the refractive index $n = 1.18$, and the incidence angle $\Theta = 41.5^\circ$. The optical length is thus $L = n \cdot d / \cos\Theta = 1360$ nm. The detection limit of the setup allows, therefore, an estimation of an upper limit of the scattering coefficient $\alpha_{sc} = 8.4 \text{ cm}^{-1}$. This upper limit for the damping might be used for the estimation of the waveguide damping with such substrates. Assuming that 10% of the modes are guided in the substrate one obtains $\alpha_{WG} = 0.84 \text{ cm}^{-1}$. This allows for sure mm-long applications.

A broad peak at around 530 nm can be seen in the reflectance spectra of non-calcined films. It is very similar to the absorption spectrum of the rhodamine 6G dye [140, 141]. The broad peak consists of two Gaussian peaks with maxima at 507 nm and 529 nm (Figure 4.26). Fluorescence measurements [142] have confirmed that the diffuse reflectance spectra of non-calcined films show photoluminescence excitation of R6G.

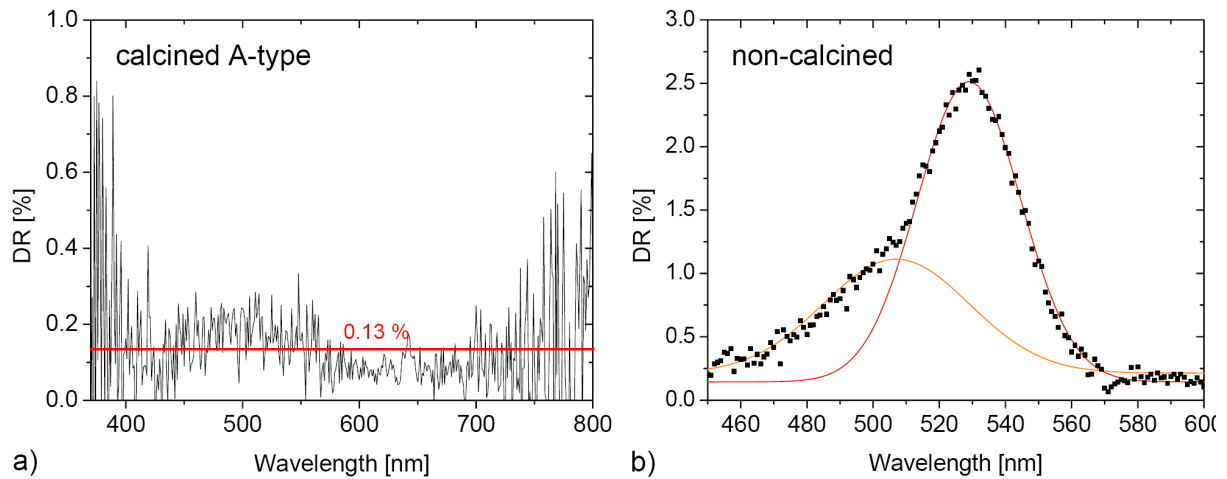


Figure 4.26: a) Magnified spectrum of the calcined A-type film BTR-BA-141-03 with the average value (red line), b) Diffuse reflectance spectrum of a non-calcined film (BTR-BA-133-05) fitted with two Gaussian peaks.

B-type films show much stronger wavelength-dependent scattering up to $S = 0.2$ (20%) as expected from the visual impression. Thicker films scatter more, due to higher concentration of the bubble-like defects. But unfortunately no mathematical

expression can be derived, because the scattering curves are superposed with the thin film oscillations of the diffuse reflected intensities guided through the film.

The most important conclusion of this section is that the calcined A-type films are very well suited for the optical applications, because of the very low optical scattering. In waveguides, a considerable part of the radiation power is guided in the evanescent field penetrating into low- n support. Therefore, it is very important that the damping due to scattering in the support is low.

4.4.2. Electrical properties

For the conductivity measurements the MSFs were deposited onto the 1.1 mm thick 12 x 42 mm glass slides coated with a conductor indium tin oxide (ITO) from Präzisionsglas & Optik GmbH. A very low ionic conductivity of $\sigma = 1.3 \cdot 10^{-8}$ S/cm was determined [143]. It is expected to be strongly dependent on ion concentration, kind of ions and humidity.

This conductivity is comparable with the lower edge of the conductivity range measured for MCM-41 [144] and the middle range of the conductivities for the zeolite faujasite [145].

4.4.3. Mechanical properties

Mechanical properties of thin films, such as hardness and elastic modulus presented in this section, can be determined interpreting nanoindentation test data. More details about this technique can be found in a review [146]. The hardness H is defined as the maximum load P_{\max} of the nanoindenter divided by the residual indentation area A on the film surface: $H = P_{\max} / A$. The hardness characterizes the resistance of a material to permanent, and in particular plastic, deformation. Under conditions of a fully developed plastic zone, the hardness H is the mean contact pressure [146]. The elastic modulus E of a material represents the relative stiffness of the material within the elastic range and can be determined from the ratio of stress to strain.

The mechanical properties were determined with nanoindentation measurements by Matthias Herrmann in the Technical University Chemnitz [147].

The following section is based on his report on these measurements. The measurements were carried out using a Nanoindenter UMIS 2000 (CSIRO) with a Berkovich diamond indenter (three-sided pyramid) and spherical diamond indenters with radii R of 1.7 μm and 48 μm .

During the nanoindentation test, the displacement of the indenter as a function of the applied force was recorded continuously in the course of a complete cycle of loading and unloading. During the loading of the indenter, the material undergoes both elastic and plastic deformation. In order to avoid the substrate influence, the hardness-depth dependence was measured using a modified Oliver and Pharr analyzing method [148]. This method consists in a series of loading cycles of the indenter to avoid thermal drift and plastic reversion. After the surface is detected, the load was increased to the maximum load and was held for few seconds in order to get a sufficient decay in case of creep process. Then the load was reduced down to 25 % of the maximum load and held constant for some time to determine thermal drift. At each maximum load (0.2, 0.3, 0.4, 0.5, 0.7 mN) 10 standard indentations were averaged [149].

A force versus displacement curve for an A-type mesoporous silica film is shown in Figure 4.27. The single measurement points are connected with a solid line forming a hysteresis loop for each maximum load. The loading curves (left branch) lie over each other for the all applied loads, but the hysteresis loop is larger for bigger loads.

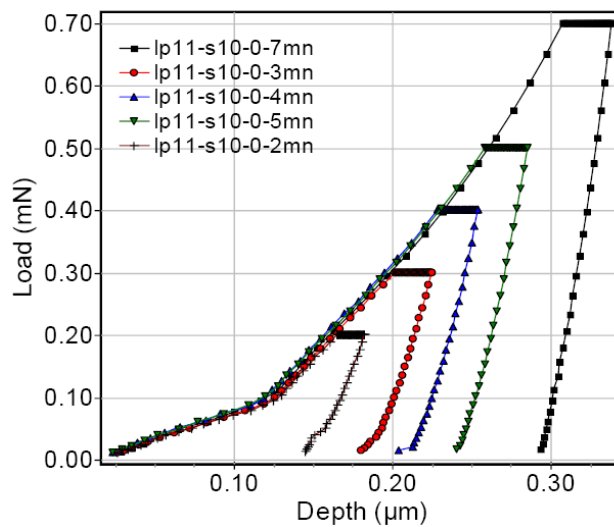


Figure 4.27: Load-depth-curves, measured with different maximum loads using a Berkovich indenter for a mesoporous films (KOD-KA-038-10) deposited on BK7 [147].

Dependence of the hardness on the ratio of contact depth h to film thickness d for the A-type mesoporous silica films deposited on the BK7 microscope slides is diagramed in Figure 4.28. The hardness is almost constant up to the ratio $h / d = 0.25$. A representative film hardness of $H = 0.20$ GPa was obtained as an average value of the first three hardness values. An h / d ratio of up to 30 % delivers a representative value of the hardness for the soft materials.

The unloading part of the curve (right branches in Figure 4.27) is essentially elastic, and with removing the plastic deformation it gives information about the elastic properties of the film. The initial slope of the unloading curve dP / dh , where P is the applied load and h is the indentation depth, is used as a measure of the contact stiffness $S = dP / dh$. The contact stiffness is used for the calculation of the indentation modulus E for each load after [146]:

$$E = \frac{1}{\beta} \frac{dP}{dh} \frac{1}{2} \frac{\sqrt{\pi}}{\sqrt{A}} \quad (4.9)$$

Here, $\beta = 1.096$ is the correction factor for a Berkovich indenter and A is the residual contact area on the sample surface. A linear extrapolation of the indentation moduli to an indentation depth of zero has been used, in order to get an approximate value for the film modulus (not shown).

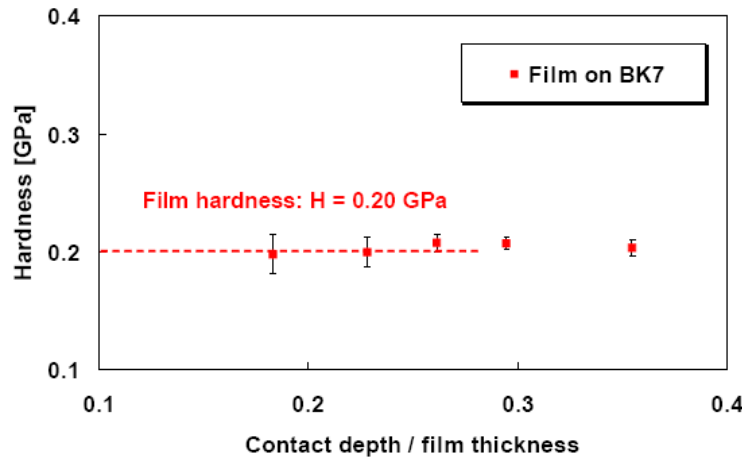


Figure 4.28: Dependence of the hardness on the ratio of contact depth / film thickness for the film KOD-KA-038-10 on BK7 [147].

An elastic modulus of $E = 2.4 \pm 0.3$ GPa has been evaluated for the A-type MSFs deposited on BK7. It is slightly lower than elastic moduli measured for other mesoporous films, $E = 3.24 \pm 0.57$ GPa for disordered sponge-like mesostructure

[150] and $E = 3.48 \pm 0.84$ for films with hexagonal domains [150]. Incorporation of pores decreases the elastic modulus significantly, but the mesoporous film in our experiments, has still had a sufficient hardness and elasticity to withstand the stresses imposed by the further treatments, especially for the application as a low-n support.

4.5. Applications of A-type films as low-n supports

The application of mesoporous films in the field of optics requires a very reproducible synthesis and constant film properties within a sufficiently narrow range. Realizations of PMMA waveguides with A-type films, waveguiding experiments and spectroscopic characterization of a demonstration device will be presented in this Chapter.

4.5.1. Coupling of light into PMMA films

In order to examine the possibility of optical wave propagation, polymethylmethacrylate (PMMA) films were deposited on the A-type MSFs as described in Chapter 3.1.3. Very transparent, clear films with no impurities and a good adherence on MSFs were obtained. The film thickness was measured with the white light interferometer assuming a refractive index of $n = 1.49$ [151]. The resulting thicknesses were in the range of 1700-2200 nm.

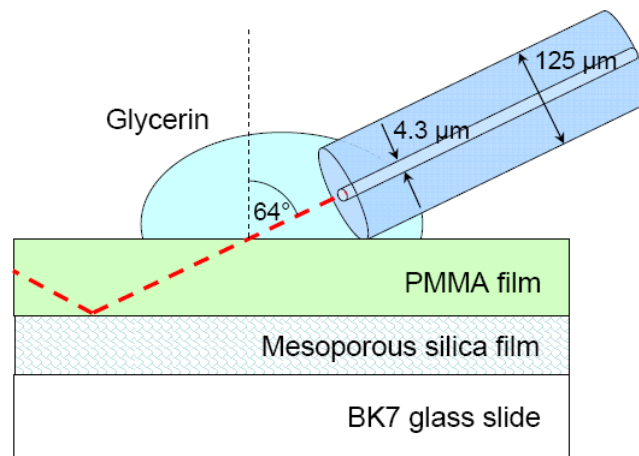


Figure 4.29: Setup for the coupling of the light into PMMA films.

The light was coupled in the PMMA film using a drop of glycerin as immersion liquid (Figure 4.29). The light coming from a halogen lamp (HL-2000-FHSA) was guided through an 1 m long optical fiber (SM 630, Soliton GmbH) with a core of 4.3 μm and $\text{NA} = 0.11$. The fiber was approximated to the film surface by the micrometer screw on a xyz micro-position holder. The approximation was observed by a stereomicroscope. The fiber was fixed on the holder at the incidence angle of 64° , which is below the angle of total reflection $\Theta = \arcsin(n_{\text{PMMA}}/n_{\text{MSF}}) = 52^\circ$, with $n_{\text{MSF}} = 1.18$ and $n_{\text{PMMA}} = 1.49$.

An artificial film defect was induced on the film surface, either a scratch or a stripe of the Scotch film. The fiber attached to the film surface with the glycerin drop was moved over the surface with the micrometer screws until the scattering of the light on the induced defect was visible under the stereomicroscope. The photos of the field of the view were made using a digital camera (Canon PowerShot A520) with 4 Megapixel at maximum resolution, ASA 400, maximum illumination time of 15 s and an aperture F3.2. The camera was fixed at the eye-piece of the microscope with a tripod holder. For the overview photos the sample was illuminated from above and the illumination time was 1/50 s.

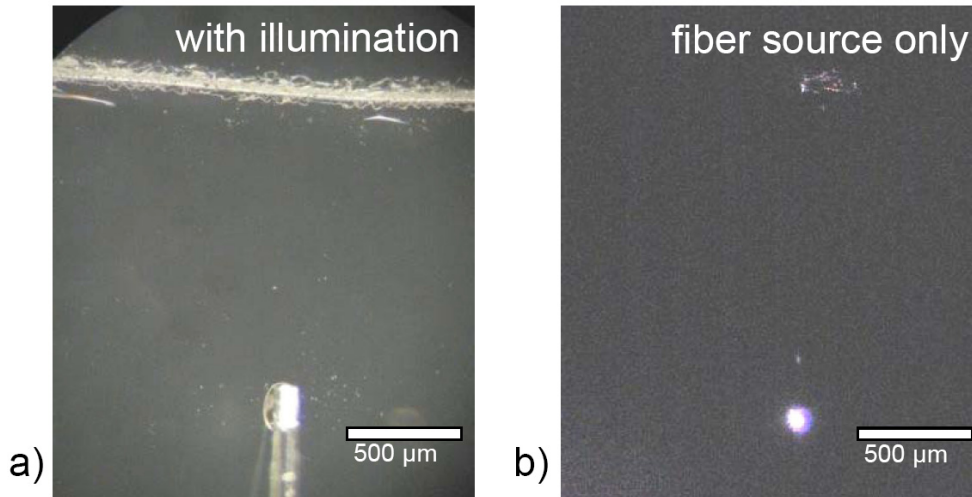


Figure 4.30: CCD image of a PMMA film on MSF (KOD-KA-074-08, $d_{\text{MSF}} = 869 \text{ nm}$, $d_{\text{PMMA}} = 2162 \text{ nm}$, $\text{RH}_{\text{MSF}} = 37.4\%$): a) with the sample illumination and b) in full darkness. The upper part of the left photo shows a scratch.

Photos of the fields of the view are presented in Figure 4.30. The photos with additional illumination show the position of the optical fiber and the induced defect

on the film surface. Photos made in full darkness show one very bright spot in the lower part of the picture. It is coming from the light scattered on the glycerin droplet. The smaller spot above is likely the beam at the glycerin / PMMA interface. In the upper part there is a broader region of light, scattered on the scratch, where the light is coupled out of the PMMA film. By moving the fiber with the micrometer screw the scattered light changes its intensity sensitively.

To exclude the possibility that the light scattered on the defect is coming from the direct beam, a barrier was placed between the coupling in and coupling out. Besides some scattering on the barrier, there is still visible intensity of the light scattered on the defect. Using another sample, an additional spot in the middle of the picture was visible. Reference experiments with PMMA films only did not show scattering on the defect. These experiments have been carried out at the same day and with the same parameters.

The changes in the intensity of the light coupled out on the defect by moving the optical fiber are probably caused by changes of the coupling-in conditions. The length and the shape of the glycerin drop change by the movement.

Because the scattering is still visible on the film defect after placement of a barrier, it cannot be assigned to the direct beam. This proves that the light is guided through the PMMA film and coupled out on the defect. An additional spot of scattering on the path between coupling-in and coupling-out visible in some photos (KOD-KA-072-06) is likely a reflection spot of the internal total reflection in PMMA. It is visible because this sample has more impurities on the surface.

Summarizing, the waveguiding capability of PMMA films on the mesoporous silica film supports was qualitatively shown in the coupling-in experiments. Quantitative statements are not possible with this method, since the intensity of the light, which is coupled out, strongly depends on the coupling-in conditions. The usage of other index-matching liquids with higher contact angle or another technique could give more reliable results for the intensity of the light coupled out in dependence on the distance. More quantitative statements for the waveguiding capability of the system polymer / MSF can be made for the system, which will be presented in the following section.

4.5.2. PhC waveguides

A finite 2D photonic crystal line defect resonator (PhC-LDR) consisting of a PMMA based polymer as the core material and MSF as the low- n substrate in the SEM micrograph in Figure 4.31 represents a result of a common project of the TU Hamburg-Harburg, IPHT Jena and MPI Mülheim. For the fabrication of these waveguides, A-type films with a thickness of 1 μm were deposited on 3 inch oxidized silicon wafers. The slab waveguide was produced by spin coating a polymer poly(methylmethacrylate / disperse red-1) (P(MMA-DR1)) onto this substrate. Some test measurements ensured that neither solvent nor polymer molecules infiltrated the mesoporous network, which would alter the refractive index of the substrate. Then 2D PhC line defect resonator structures were realized by electron beam lithography (EBL), reactive ion etching (RIE), and dry etching [152] in the IPHT Jena. Only the 1.5 μm thick PMMA film was etched, so that the air holes do not penetrate the MSF substrate. The final resonator consisted of two finite hole arrays separated by a non-structured region. The lattice defect is formed by omitting 4 lines of holes perpendicular to the wave propagation direction. A 150 nm hole radius was chosen, which results in an optical stop band around the vacuum wavelength of 1.3 μm . The exact design of the structure was optimized by simulations using a 3D finite integration technique as described in [13].

The simulations showed that although the core has a moderate refractive index of $n = 1.54$, the refractive index contrast is sufficient to achieve nearly symmetrical field patterns. No deep etching into the substrate was assumed, but hardly any radiation losses into the substrate were observed, due to high vertical index contrast in this quasisymmetrical PhC slab.

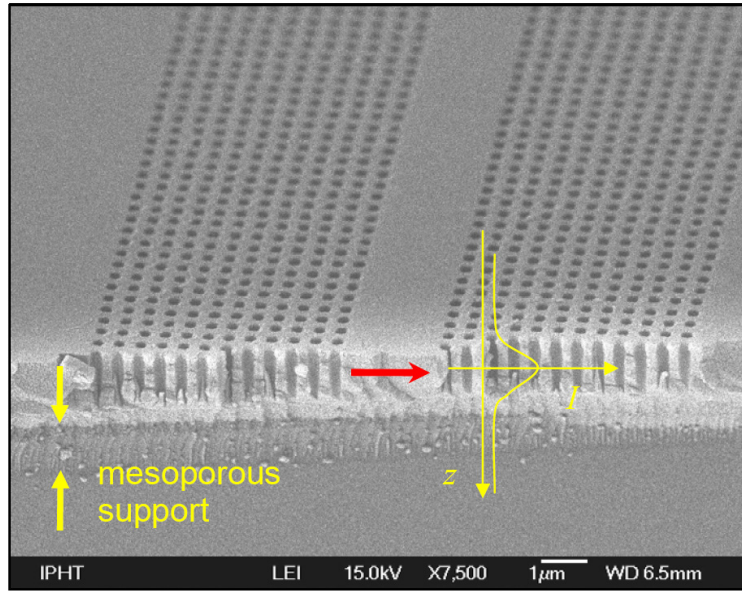


Figure 4.31: SEM micrograph of the realized 2D PhC line defect resonator made of *P(MMA/DR-1)* on an A-type mesoporous silica film as a support [13]. A schematic drawing shows the field distribution in a guided mode (arrow) which penetrates into the support.

Beside the simulations, a simpler consideration can be used to predict the field confinement in the waveguide. The decay of the guided modes into the support is depicted in the Figure 4.32. The decay depth depends on the mode type, waveguide thickness, and significantly on the refractive index of the support. This effect can be estimated by a lower limit of the field decay as shown in Figure 4.32. The fields of every guided mode of a homogeneous waveguide decay slower into the support than

$$E \approx E_0 \exp \left\{ -z \cdot 4\pi \sqrt{n_{\text{core}}^2 - n_{\text{sup}}^2} / \lambda_0 \right\} \quad (4.10)$$

with the penetration depth z , the refractive index n_{core} of the core (PMMA), the refractive index n_{sup} of the support (MSF), and the wavelength λ_0 of the used light [153]. This estimation delivers the result that a 1 μm thick mesoporous film can be sufficient for the field confinement, but not a Teflon film with $n = 1.3$ since there is still a remarkable field intensity at 1 μm which can be absorbed or irradiated.

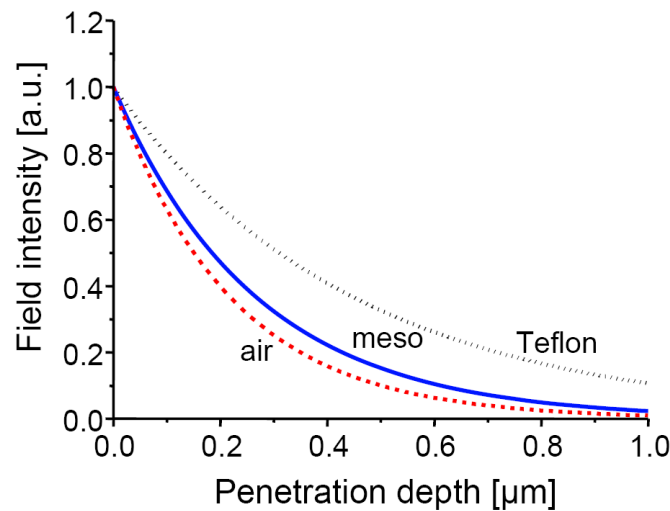


Figure 4.32: The penetration of waves into different waveguide supports (air, mesoporous film, or Teflon). The curves show the minimum decay of the field intensity into the supports from a waveguide with an effective refractive index of 1.38 which is relevant for the 2D PhC waveguide.

The transmission spectra of the P(MMA/DR-1) / MSF 2D PhC line defect resonator were measured in TU Hamburg-Harburg for different polarizations by the prism coupling method [154]. A spectrum taken from an unstructured part of the slab was used as a reference. By this way only the spectral response of the PhC-LDR was extracted. A transmission spectrum of this line defect resonator is given in Figure 4.33. A band gap between 1250 nm and 1460 nm is clearly visible. Within the band gap a defect state belonging to the resonator can be detected. The finesse of the resonator is remarkably high, which is also an effect of the used mesoporous substrate. The resonator structure on the mesoporous substrate showed a high transmission in the resonance peak. It amounts about 57% for the transversal electric (TE) and 78% for the transversal magnetic (TM) polarization compared to that at the dielectric edge. These values were expected from the simulations (60% for TE and 82% for TM mode) and exceed values determined on similar structures on conventional Teflon supports. However, the defect peak is wider than expected. This can be explained by the conical shape of the holes, which leads to inhomogeneous broadening of the Lorentzian transmission function. A second peak on the left part of the band gap is related to higher vertical mode. A further interesting property of this transmission spectrum are the seemingly absent

radiation losses at the air band side of the band gap. The transmission has the same height at this band edge as at the dielectric edge. In contrast, the PhC waveguides on Teflon show strong losses at the air band edge since these states are above the light cone [13].

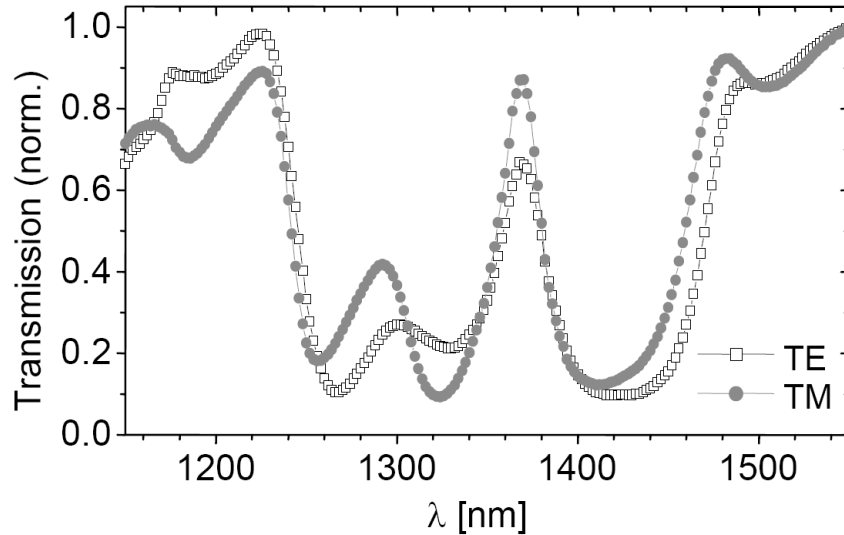


Figure 4.33: Transmission spectrum of a $P(\text{MMA/DR-1})$ / MSF line defect resonator for TE-like and TM-like modes. The high transmission at the resonance wavelength and the low losses on the air band side indicate a strong confinement of light inside the slab waveguide core [13].

With the work described in this section, a new concept of quasisymmetric optical photonic crystal slab waveguide was introduced. With the use of the mesoporous solid substrate with an ultra-low refractive index, the light line is lifted up almost to the highest possible extent. Deep etching into the substrate was not necessary to suppress radiation losses. The vertical symmetry, which leads to a decoupling of the modes, could be further improved by the use of the core materials with higher refractive index.

4.6. PZT Films

Up to now there is no good material which can be used for electro-optically switchable PhCs. The ferroelectric lead zirconate titanate films (PZT) are very promising for the realization of optical switches, which are key elements of integrated optics.

The thin films of PZT have been fabricated by a sol-gel technique as described in Chapter 3.1.4. Their characterization will be presented in the following section. The transparency of the PZT films deposited on glass will be characterized by use of an UV-Vis spectrometer and the possibility of their thickness tuning will be examined. The PZT films deposited as an overlayer on the mesoporous silica films (MSFs) will be compared with the PZT films on glass and Si-wafer as a verification of their compatibility with MSFs. Finally, one possibility for the structuring of PZT photonic crystals will be presented.

4.6.1. Characterization of PZT films

All as-deposited PZT films were very transparent and homogeneous with at most some dust inclusions. The calcined films were also very transparent and clear (Figure 4.34 left) and seem to be better than other PZT films [86]. The transmission and reflection spectra (Figure 4.34 right), measured with the UV-Vis spectrometer and the white light interferometer, respectively, show oscillations typical for thin layer interference. The sum of transmission and reflection is about 95%. Estimated systematic error of these two methods is maximal 1%. It means that about 5% of the light is scattered or absorbed.

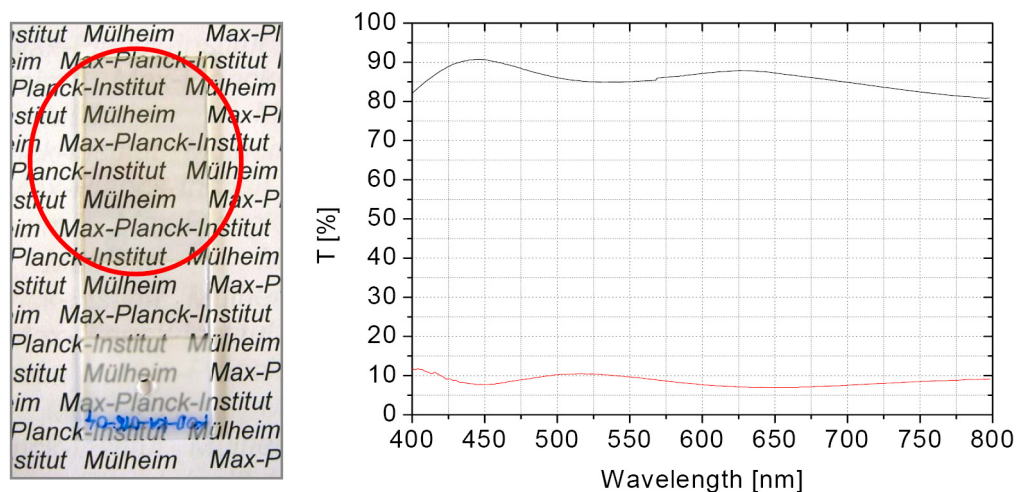


Figure 4.34: Left: Photograph of a PZT film (KOD-KA-016-04) made with a digital camera (Casio Exilim Z30 at 72 dpi, illumination time of 1/160 s, and an aperture F2.8). The brightness and the contrast were automatically adjusted. Right: Transmission (black) and reflection (red) spectra with typical thin film oscillations.

Closer observation of the films with an optical and electron microscope reveals an dense crack network (Figure 4.38 a). The cracks are straight with well defined angles between them.

As discussed in many publications, e.g. [88], the stress in films is the cause of the cracking, developing in gel films on firing. In our synthesis it was however expected that the strong hydrogen bonds between the amide groups of PVP and the hydroxyl groups of the metalloxane polymers could hinder the condensation reaction in films, promoting the stress relaxation in the heating-up stage [88]. Although the crack formation was indeed reduced by addition of PVP, it could not be fully eliminated during the calcination in the electric furnace. This fact can be assigned to the different thermal expansion coefficients of PZT and the support. Therefore the final tuning of the PZT film properties have to be adjusted to the support system.

Different heating rates did not have big influence on the final product. No influence on the optical appearance of the films was noticed by microscopical observation. The most sensitive step in the fabrication is the crystallization at high temperatures, at which the cracking occurs.

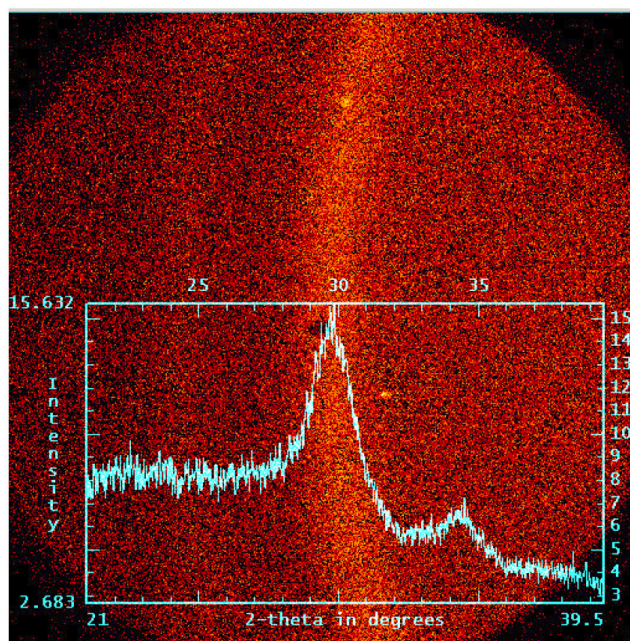


Figure 4.35: XRD pattern of a PZT film (BTR-BB-161-06) recorded for 2h at the incidence angle $\omega = 0.4^\circ$. The inset is the pattern obtained by the area integration from $2\theta = 21^\circ$ to $2\theta = 39.5^\circ$.

The XRD pattern of a PZT film in Figure 4.35 was obtained by use of the GADDS setup (see Chapter 3.4.1) at the detector position of $2\Theta = 30^\circ$. The 1D pattern resulting from the area integration shows two pronounced diffraction peaks at the positions $2\Theta = 29.7^\circ$ and $2\Theta = 34.4^\circ$. The position of the peaks is in a good agreement with other XRD patterns for PZT, e.g. $2\Theta = 30^\circ$ and $2\Theta = 34.2^\circ$ in [155], but the peaks are broader than there. The full width at half maximum (FWHM) of the peak at $2\Theta = 29.7^\circ$ is $\beta = 1.74^\circ$. Using Scherrer equation:

$$L = \frac{0.94 \cdot \lambda}{\beta \cdot \cos \Theta} \quad (4.11)$$

with the wavelength of the $\text{CuK}\alpha_1$ radiation $\lambda = 1.54 \text{ \AA}$, the crystallite size can be calculated to $L = 5.1 \text{ nm}$. The position of the diffraction peaks is a good indication that the known PZT structure [78] is realized in these small crystallites as well.

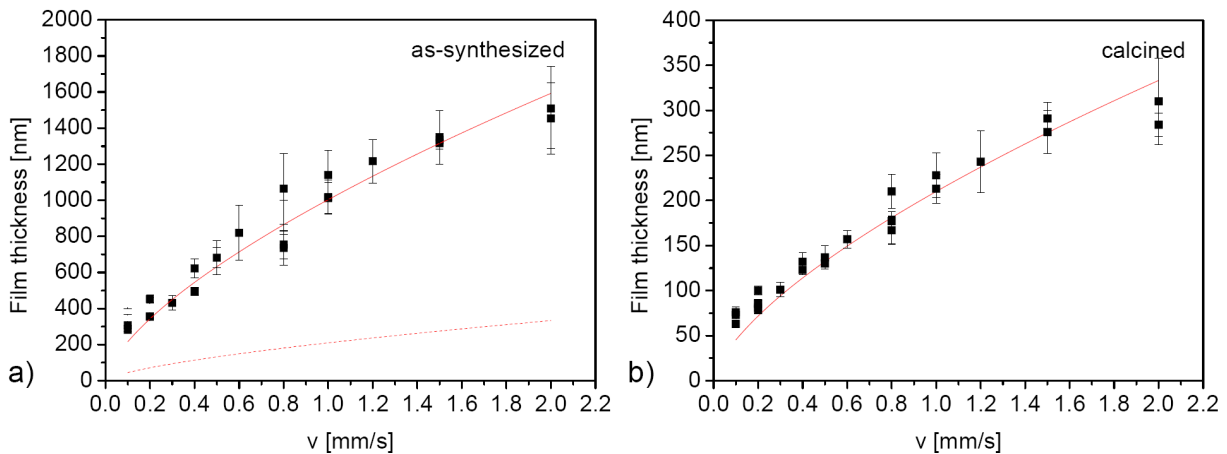


Figure 4.36: Film thickness in dependence on the drawing rate v for a) as-synthesized and b) calcined PZT films. The data were fitted with the function $a \cdot v^{2/3}$.

The film thickness was measured with the white light interferometer before and after thermal treatment. The refractive index of $n = 2.56$ from the literature [82, 89] was assumed for both, as-synthesized and calcined samples. Reflection curves of as-made films could be fitted without problems, whereas for the calcined films it was more difficult, because the curves for very thin films exhibit only two extrema. The film thickness as a function of the drawing rate in Figure 4.36 follows a $v^{2/3}$ dependence, which was derived in the Landau-Levich theory in Chapter 2.5.2.

The film thickness decreased significantly upon calcination (dotted line in Figure 4.36 a). A shrinkage to the 26% of the film thickness before thermal treatment was

averaged for all measured films. Such large shrinkage was also reported from other preparations and has been estimated to 29% [155] and 32% [156]. The large contraction of the films is caused by evaporation of rests of Methoxyethanol (boiling point: 124.5°C) and acetylacetone (boiling point: 139°C) as well as the decomposition of PVP during the thermal treatment.

This investigation showed that the thickness tuning is also possible for the PZT films. However, all films deposited on glass or Si substrates show dense crack networks.

4.6.2. PZT films on MSFs

PZT films were deposited on the mesoporous silica films (MSFs) in the same manner as on the glass or Si supports. They were also transparent and mostly clear. The interference colors, typical for thin films, are visible in the insets in Figure 4.37. The unique color indicates a good homogeneity of the film thickness. Only the borders, especially the outflow edge, show different colors, due to changes in the film thickness. As the film is very thick at the outflow edge, it starts to peel off [115].

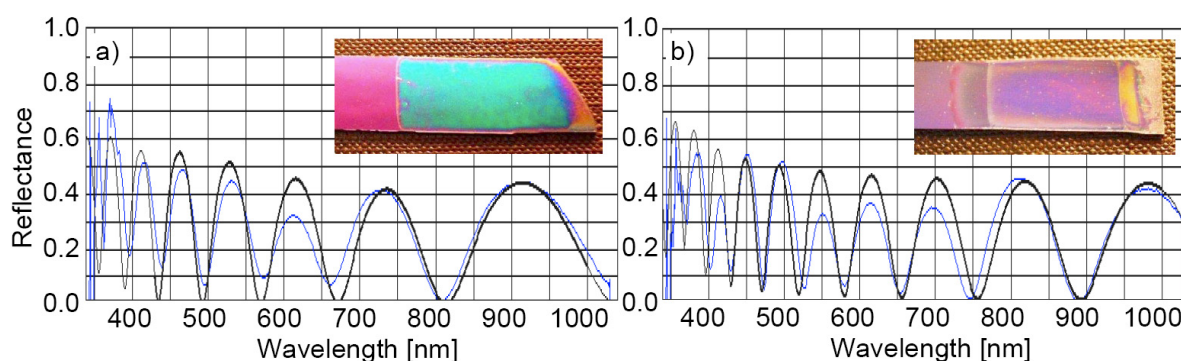


Figure 4.37: Measured and calculated reflection spectra of the PZT films on a) Si-wafer (KOD-KA-056-04) and b) mesoporous silica film (KOD-KA-055-12). Insets are photographs of PZT on Si-wafer and on MSF, respectively. The photographs of the calcined samples were made using a digital camera Casio Exilim Z30 at 72 dpi, illumination time of 1/50 s, and an aperture F3.5 by diffuse sample illumination [115].

Observation with an optical microscope, as in Figure 4.38, showed that the PZT films deposited on the MSF have much less cracks, mostly sporadic star-like film disturbances. However, the surface has blur regions, not visible in the photography

and microscope pictures. It is possible that the mesoporous film changed or even crashed during this treatment.

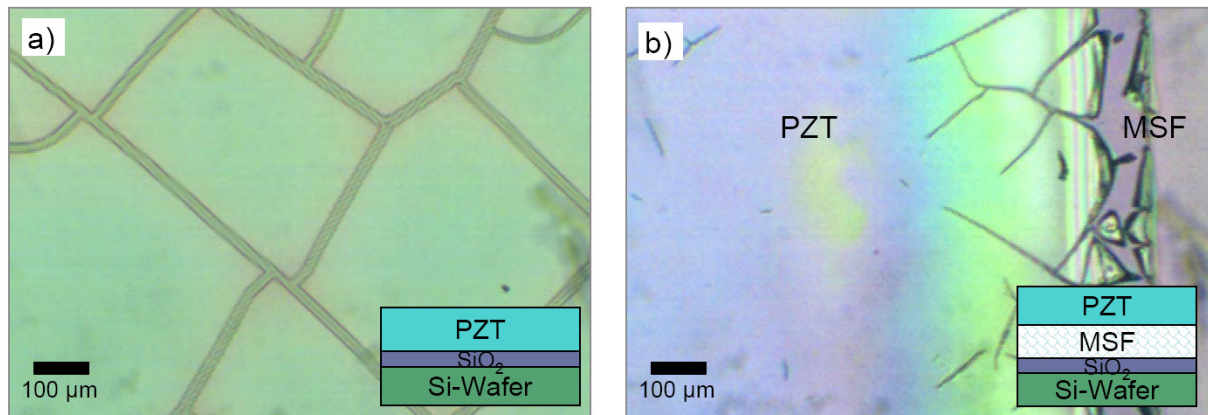


Figure 4.38: Microscope pictures of a PZT film deposited on a) silicon wafer (KOD-KA-051-01) and b) mesoporous silica film (KOD-KA-053-03). The photos were made using an eye-piece camera (MA88, CA Scientific Co) with 640x480 pixels [115].

Thickness measurements (Figure 4.37) indicated that the thickness d of the MSF is 31% lower after the deposition of PZT. Such a reduction of the film thickness might be caused by infiltration of the PZT precursor and a resulting break-down of the mesostructure. Possibilities to avoid such effects could be the change of surface properties of the MSF or the introduction of surface barriers [157].

The suppression of the regular crack formation on MSF supports is however an encouraging result on the way to high-quality PZT films. The flexibility of the porous structure likely lowers the stress induced in the PZT by the high temperature treatment.

4.6.3. Structuring of PZT

After the vertical structuring, i.e. film formation, a lateral structuring or periodic pattern formation is required for the fabrication of PhC slab waveguides. A lateral structuring possibility for the PZT films is e.g. RIE with CCl₂F₂ [158]. An alternative for the conventional lithographic techniques could be templating methods in a sol-gel process. Opals and inverse photonic crystals made of them can be used as a demonstration.

Opal films were prepared by Dr. Hong-Liang Li using the capillary deposition method [159]. Here, a colloid suspension of 10 wt.% polystyrene (PS) spheres (Duke Scientific) with the size of 277 nm was dispersed into deionized water as a 0.5 wt.% suspension. The suspension was deposited via a capillary tube in-between two glass slides forming capillary cell. The PS spheres self-assembly by drying into a solid opal film with the thickness of 75 μm , determined by the spacer between the two slides.

The dried opal templates were infiltrated with the PZT solutions using the same setup. Due to the capillarity, the PZT solution filled the capillary tube, and then it was relayed by the capillarity of the two-slide capillary cell and filled the voids between PS spheres. The solution, having infiltrated into the film, was then concentrated upon the solvent evaporation, while the capillary tube compensated the solution loss continuously. After the infiltration for 49 days and subsequent drying in air for another 17 days the films were heated to 550°C in order to remove the PS template and solidify the PZT network.

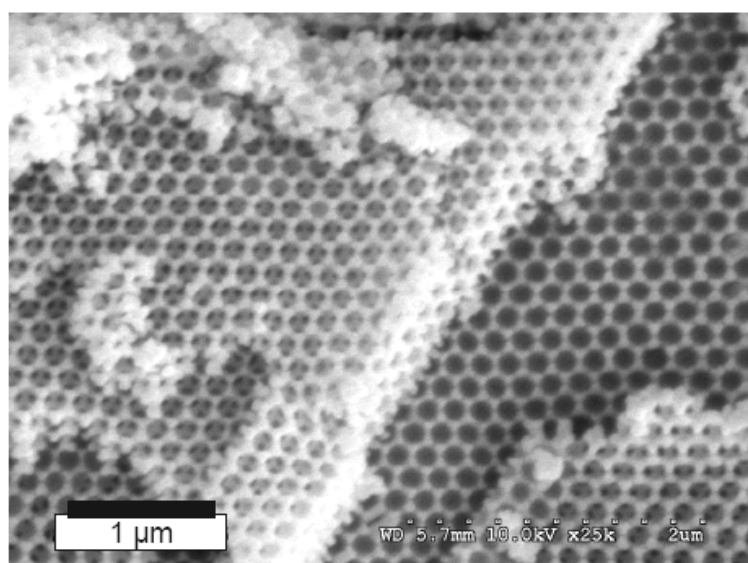


Figure 4.39: A SEM micrograph of an inverse opal of PZT recorded at 10 kV with 25000x magnification.

Investigations with the scanning electron microscope (SEM) show an inverse structure between the residual volume structure (RVS) and the skeleton structure (SkS) [160]. The honey-comb-like hexagonal ordering of the voids in the skeleton is formed due to fcc packing of the PS spheres, which were in the place of voids

before calcination. The inverse structure was found in all investigated samples containing different amounts of PVP, but the most regular skeleton structure seems to be formed in the sample without PVP (Figure 4.39). The periodicity of the voids is about 200 nm, which is about 28% smaller than the size of the PS template spheres. The reason for this fact is a considerable shrinkage of the structure during the calcination.

However, the films of inverse opals are very brittle, they crack during calcination into pieces with sizes of few hundred micrometer. The large shrinkage of the gel during calcination is certainly the main reason for the cracking. The possibility of the extension of the inverse opals to thin layers remains still a challenging open question.

A report about inverse opals of a similar ferroelectric dielectric $(\text{Pb},\text{La})(\text{Zr},\text{Ti})\text{O}_3$ (PLZT) has been published in [161]. Also this work shows the possibility to structure PZT-type ferroelectrics with a templating method. This method might be applied to PhC systems if the conventional lithographic techniques do not succeed to reach the required accuracy.

4.7. Structure determination of related materials

The small angle X-ray scattering (SAXS) measurements using the GADDS system (Bruker AXS) were successfully applied for the structure determination of other materials. Most closely related materials are the spin-coated mesoporous silica films presented in the following section. Their characterization allows direct comparison with the dip-coated MSFs, which are the main topic of this thesis. Another range of materials are the ordered arrays of silica particles. They represent another morphology of mesoporous silica, which are prepared in a similar synthesis class.

4.7.1. Spin-coated BRU-type mesoporous films

This kind of mesoporous silica films was fabricated by Bruinsma with a procedure modified from [162]. We call these films BRU-type. The precursor solutions were prepared by combining cetyltrimethylammonium chloride (CTACl),

deionized water, ethanol, hydrochloric acid and tetraethyl orthosilicate (TEOS). TEOS was added after the surfactant was completely dissolved. The solutions were aged for about an hour prior to coating. The cover slide substrates were flooded with spin-coating solution and spun at 3000 rounds per minute with the maximum acceleration. The films were exposed to the ammonia atmosphere in the closed Petri dishes for 15 min in order to increase silica condensation. Then the films were heated at 105°C overnight in air and calcined at 450°C for 5-10 minutes. The films are fully transparent (Figure 4.40 a).

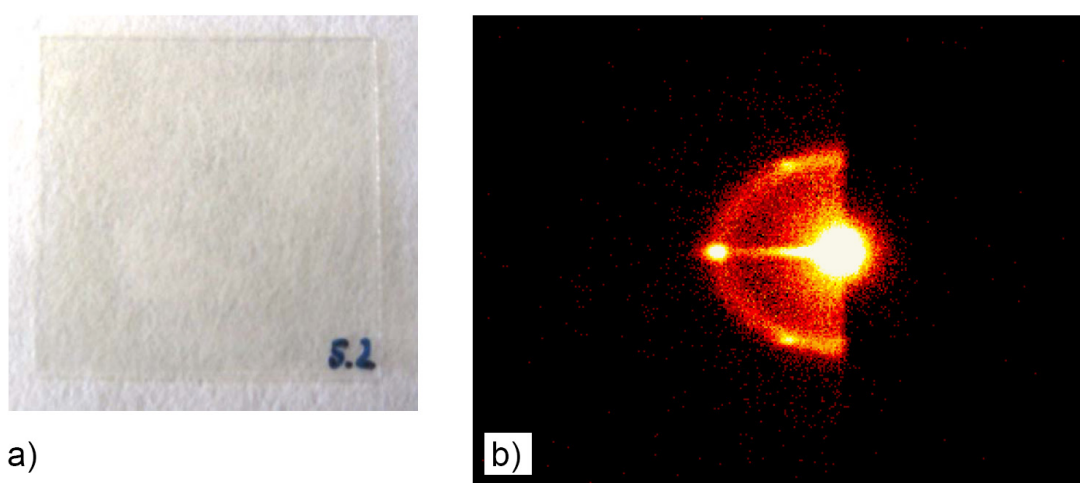


Figure 4.40: a) A photograph of a BRU-type mesoporous silica film made by a digital camera (Casio Exilim Z30) at 180 dpi, illumination time of 1/40 s, and an aperture F2.6. The film is deposited onto the whole surface of the cover slide by spin-coating. b) 2D SAXS diffraction pattern of a BRU-type film recorded at the incidence angle of $\omega = 0.1^\circ$ for 30 minutes.

Figure 4.40 b) shows a 2D SAXS diffraction pattern of such a film. The right side of the pattern is covered by the sample, which was positioned perpendicular to the image plane. The large bright spot in the middle of the pattern is parasitic scattering from the pinholes and the beam-stop. Two different scattering features coming from the film can be distinguished: well-defined diffraction spots and a diffuse ellipse. The ellipsoidal diffraction pattern has a long half-axis of $2\Theta = 2.58^\circ$ and a short half-axis of $2\Theta = 2.02^\circ$. Using the Bragg equation (4.1) the periodicity was calculated to 3.4 nm for the long half-axis and 4.4 nm for the short one. There are three very pronounced Bragg peaks visible on the ellipse with an azimuthal angle of about 60° between them.

The nearly sixfold symmetric diffraction pattern indicates 2D hexagonal mesostructural ordering [120]. The most intense diffraction spot, the equatorial Bragg reflection (001) is assigned to the organization of the cylindrical micelles with the axes preferentially aligned parallel to the surface plane. All three Bragg spots are superposed to the continuous ellipse, which is usually [52] attributed to the wormlike structure. It means that some cylindrical micelles are organized into domains that are not well-aligned with the surface of the film, but with the axes randomly oriented, as suggested by the continuity of the diffraction ellipse. The ellipticity of this ellipse of 1.28 is a result of the uniaxial contraction perpendicular to the film surface. Therefore, the superposed ordered structure can be considered as the 2D centered-rectangular porous structure with the planar space group $c2mm$, which is a deformation of the hexagonal structure with the space group $p6mm$.

4.7.2. Mesoporous silica particles

The mesoporous silica particles grown on the patterned surfaces were prepared by Ahmed Khalil and the procedure is described in detail in ref. [163]. The used silica synthesis class, SBA-3 [164], has similarities to the synthesis for the preparation of the BRU-type films. The specific arrays of mesostructures (Figure 4.41 a) were grown on the glass slides surfaces patterned by microcontact printing of self-assembled monolayers.

The SAXS measurements were performed at the incident angle of $\omega = 0.2^\circ$ between the beam and the support plane. The pattern in Figure 4.41 was recorded for 5 hours and the measured sample region was about $100\ \mu\text{m} \times 5\ \text{mm}$. Beside parasitic scattering, three very pronounced reflection spots are visible at an angle of $2\Theta = 2.28^\circ$ with an azimuthal angle of $\varphi = 60^\circ$ between them. The distance from the center of the non-diffracted beam indicated by the cross is the same for all spots. The periodicity was calculated using Bragg equation to $d_s = 3.9\ \text{nm}$. There are also three other spots with lower intensities visible in the pattern. They are higher order reflections. The additional spot at $2\Theta \approx 2.6^\circ$ is a peak doubling, which occurs as a reflection of the fundamental beam on the support surface. Its position depends on the incident angle.

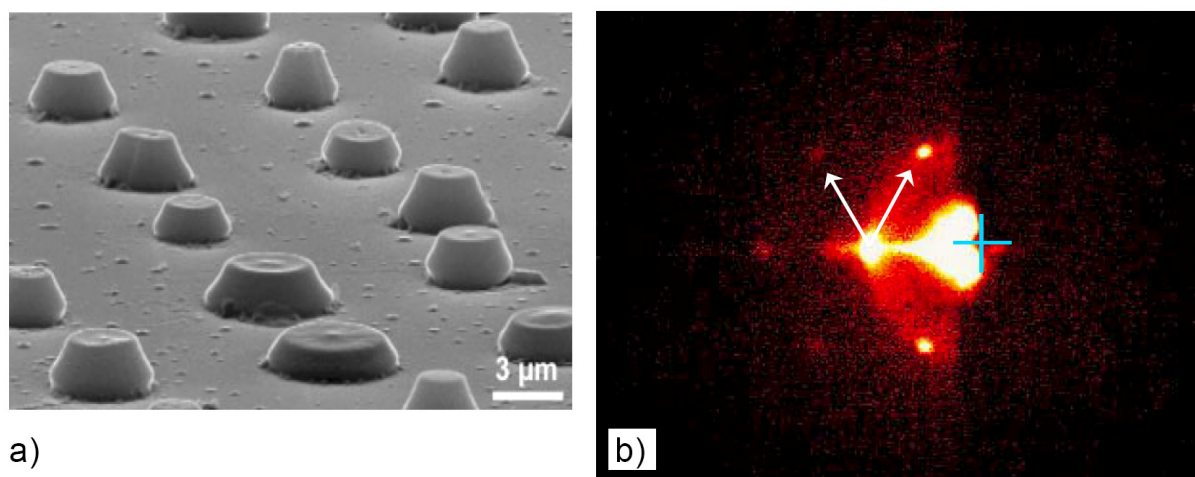


Figure 4.41: a) SEM micrograph of a particle array viewed tilted by 80° (from [163]). b) 2D SAXS diffraction pattern of an as-made particle array recorded at the incidence angle of $\omega = 0.2^\circ$ for 5 hours. The two arrows indicate the direction of the reciprocal lattice and the cross indicates the position of the non-diffracted beam (analogous to [163]).

The sharpness of the reflection spots and higher order spots indicate a high degree of mesostructure ordering. Furthermore, the only one set of sharp spots, i.e. only one d -spacing, proves an identical structure for most of the particles in the array exposed to the X-ray beam.

The spots are hexagonally ordered, but their intensities show pronounced deviations from the hexagonal symmetry. A similar pattern was measured for the mesoporous fibers prepared by the same synthesis [165]. The pattern was explained by the circular reciprocal space structure consisting of a system of rings. The surface of the Ewald sphere intersects these rings over a relatively large range of angles. The 2D cut in the Fourier space thus always results in sharp spots in the diffraction pattern. The difference in the pattern in Figure 4.41 is that the spots in the hexagonal lattice are rotated by 90° compared to the pattern in [165]. This finding can be explained by different channel packing for the fibers and particles. In both cases the channels of about 4 nm in size, as derived from the SAXS measurements, coil around the central axis of either fibers or particles. Whereas the adjacent channels form a linear stack parallel to the symmetry axis of the fibers, they form a linear stack parallel to the support in the case of the particles. A more detailed description of these differences can be found in [166].

Due to their circular symmetry, these objects are called “circulites” and represent a novel class of hierarchical solid state organization [166]. The array of such particles opens many new options for optical, electrical, and mechanical investigations and represents a good example for the combination of bottom-up and top-down techniques. The organization of the materials on different length scales is of particular interest for optical devices.

4.7.3. Common aspects of the investigated mesostructured materials

Mesoporous silica films with other structures, such as BRU-type films, are also a good candidate as a low- n substrate, but potentially the refractive index is not as low as for the A-type films. The refractive index of the mesoporous spheres, made by use of the same structure directing agent CTACl, was measured to $n = 1.22 \pm 0.06$ in [167]. The d -spacings in the XRD pattern of a BRU-type film are lower than in the case of A-type films indicating lower porosity and, therefore, lower refractive index. However, these films are also very clear without any defects and cracks and by visual appearance comparable to A-type films.

It was previously believed, that a certain synthesis of mesostructured materials always results in a certain structure of the material. But, these syntheses, such as SBA-3 and SBA-15 can be rather considered as synthesis classes, resulting in materials with different morphologies and different structures. Partially they can be regarded as frozen non-equilibrium states. These new structures have been shown in examples of mesoporous particles, as a special case of the SBA-3 synthesis class, and B-type films as a new structure of the SBA-15 synthesis class. These examples show still open possibilities to explore the known synthesis classes and direct them on the way to the desired materials.